AD-A120 951 A MODEL OF VERTICAL DISPERSION OF INERTIAL WAVES IN THE 1/1
UPPER OCEAN(U) SCIENCE APPLICATIONS INC MCLEAN VA
D M RUBENSTEIN AUG 82 SAI-83-861-WA N00014-82-C-0243

UNCLASSIFIED F/G 8/3 NL

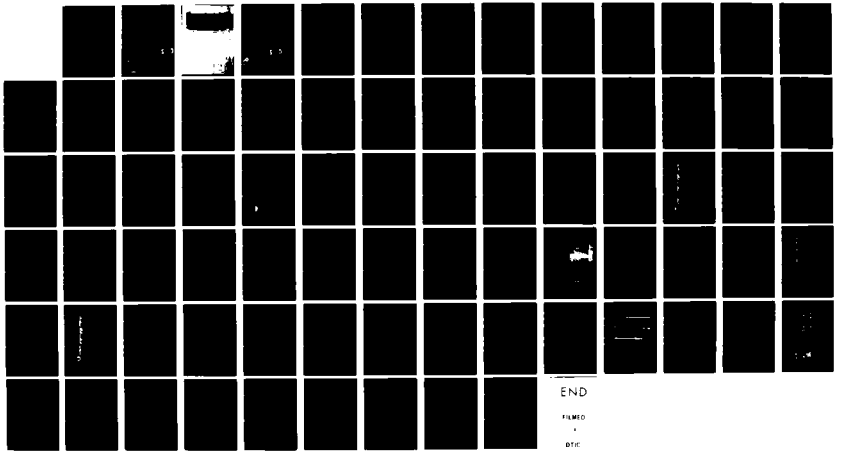

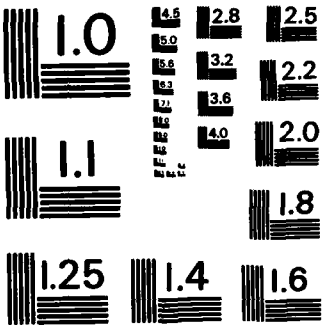

MICROCOPY RESOLUTION TEST CHART
NATIONAL BUREAU OF STANDARDS-1963-A

AD A120951

(12)

DTIC FILE COPY

DTIC ELECTE NOV 02 1982 D

SCIENCE APPLICATIONS, INC.

82 11 02 041

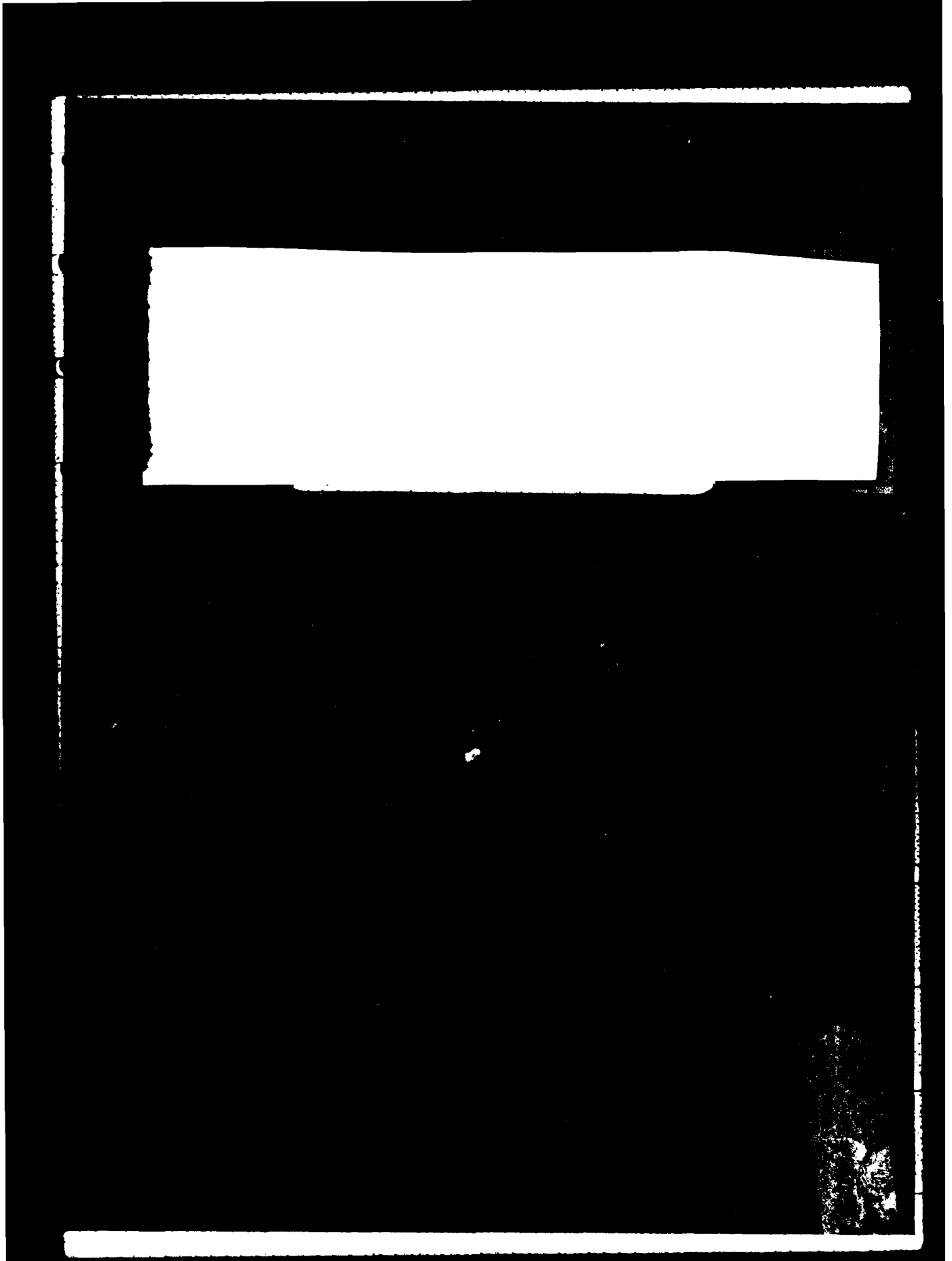

Table 1.1

12

A MODEL OF VERTICAL DISPERSION OF INERTIAL WAVES IN THE UPPER OCEAN

SAI-83-861-WA

SCIENCE APPLICATIONS, INC.
Post Office Box 1303, 1710 Goodridge Drive, McLean, Virginia 22102, (703) 821-4300

A MODEL OF VERTICAL DISPERSION OF INERTIAL WAVES IN THE UPPER OCEAN

SAI-83-861-WA

OPD-TR-82-033-01

November 1982

Prepared by:
David M. Rubenstein

Prepared for:

Naval Ocean Research and Development Activity
Ocean Measurements Program, Code 540
NSTL Station, Mississippi 39529

Final Report for Contract No. N00014-82-C-0243

SCIENCE APPLICATIONS, INC.

1710 Goodridge Drive
P.O. Box 1303
McLean, Virginia 22102
(703) 821-4300

UNCLASSIFIED

SECURITY CLASSIFICATION OF THIS PAGE (When Data Entered)

REPORT DOCUMENTATION PAGE	READ INSTRUCTIONS BEFORE COMPLETING FORM
1. REPORT NUMBER: SAI-83-861-WA	2. GOVT ACCESSION NO.: AD-A120951 / 3. RECIPIENT'S CATALOG NUMBER:
4. TITLE (and Subtitle): A Model of Vertical Dispersion of Inertial Waves in the Upper Ocean	5. TYPE OF REPORT & PERIOD COVERED: Final Report 1/82 - 8/82
	6. PERFORMING ORG. REPORT NUMBER: SAI-83-861-WA
7. AUTHOR(s): David M. Rubenstein	8. CONTRACT OR GRANT NUMBER(s): N00014-82-C-0243
9. PERFORMING ORGANIZATION NAME AND ADDRESS: Science Applications, Inc. 1710 Goodridge Drive, P.O Box 1303 McLean, Virginia 22102	10. PROGRAM ELEMENT, PROJECT, TASK AREA & WORK UNIT NUMBERS
11. CONTROLLING OFFICE NAME AND ADDRESS: NORDA Code 540 Ocean Measurements Program NSTL Station, Bay St. Louis, MS 39529	12. REPORT DATE: August 1982
	13. NUMBER OF PAGES: 72
14. MONITORING AGENCY NAME & ADDRESS (if different from Controlling Office)	15. SECURITY CLASS. (of this report): UNCLASSIFIED
	15a. DECLASSIFICATION/DOWNGRADING SCHEDULE

16. DISTRIBUTION STATEMENT (of this Report)

Approved for public release; distribution unlimited

17. DISTRIBUTION STATEMENT (of the abstract entered in Block 20, if different from Report)

Approved for public release; distribution unlimited

18. SUPPLEMENTARY NOTES

19. KEY WORDS (Continue on reverse side if necessary and identify by block number)

Inertial Oscillations
Inertial Waves
Upper Ocean
Internal Waves
Dispersion
Ocean Model
Mixed Layer

20. ABSTRACT (Continue on reverse side if necessary and identify by block number)

See Reverse Side

DD FORM 1 JAN 73 1473 EDITION OF 1 NOV 65 IS OBSOLETE

UNCLASSIFIED

SECURITY CLASSIFICATION OF THIS PAGE (When Data Entered)

ABSTRACT

A linear model of the vertical dispersion of near-inertial waves is developed. A porosity distribution near the bottom of the computational domain minimizes bottom reflections, and simulates an ocean of infinite depth. The model is used to show that the vertical dispersion of near-inertial waves in the upper ocean is sufficient to account for the observed rapid decay of inertial oscillations in the surface layer. When the upper pycnocline is sufficiently peaked, a resonant frequency interference effect is predicted. This effect modulates the dissipation of surface layer inertial oscillations, and their magnitude after a storm need not decay monotonically. We look at deep-ocean observations taken during MILE, and find some suggestive evidence of this interference effect. We also compare model simulations with Baltic Sea observations made by KRAUSS (1981), and show that near-inertial waves reflect off the shallow (105 m) bottom within a few inertial periods after a storm.

TABLE OF CONTENTS

LIST OF FIGURES

LIST OF FIGURES (cont.)

LIST OF TABLES

Section 1
INTRODUCTION

1.1 BACKGROUND

Records of currents in the upper ocean are often dominated by intermittent oscillations at the inertial frequency. It is well known that the strongest of these oscillations are wind driven. A sudden change (over a time scale less than f^{-1}) in the local wind stress will generate inertial oscillations in the ocean's near-surface layer. These oscillations then decay within a few days. The dissipation mechanism is not yet fully understood. In this report we demonstrate the likelihood that vertical dispersion of low frequency internal waves is responsible, at least in part, for the dissipation of inertial oscillations.

Several investigators have shown that inertial oscillations in the surface layer are largely due to wind forcing. POLLARD and MILLARD (1970) compared the inertial oscillations computed using a simple horizontally homogeneous wind-driven model with upper ocean current observations. The action of the wind on the mixed layer was imposed as a body force. To dissipate the inertial oscillations and to obtain approximate agreement, it was also necessary to introduce an artificial linear damping term. Best comparisons were obtained when the e-folding decay time of the damping term was in the range two to eight days. The implication is that this damping term is a gross parameterization of a certain process (or processes) which can remove energy from the mixed layer.

It is not yet clear what type of process dominates the dissipation of inertial energy in the surface layer. During a wind event, strong shear near the inertial frequency, just below the base of the mixed layer, causes the thermocline interface to erode. KRAUSS (1981) showed, from observations in the Baltic Sea and from numerical results, that the Richardson number over a 10 m interval across the interface is driven below 1/4 during storms. Mixing due to breaking internal waves or shear instability induces entrainment of momentum across the thermocline interface. The deepening of the mixed layer distributes momentum over a greater volume, and inhibits the unlimited growth of inertial oscillations.

Nonlinear interactions may help to dissipate inertial waves. KRAUSS (1981) cites observations of inertial waves below the Ekman layer with amplitude ~40 cm s^{-1}, and horizontal wavelength ~100 km. Thus, at the latitude 56°N, the nonlinear advection term $u\partial u/\partial x$ is about 10% of the Coriolis term fu. To this extent then, the inertial waves are themselves nonlinear. The resultant super-inertial frequency motions generate internal waves which are free to propagate downward through the thermocline. Spectral analysis of moored current meter records yields some evidence of nonlinear interactions. Harmonics at twice the inertial frequency (KRAUSS, 1981) and at multiples of the inertial and semidiurnal frequencies (DAVIS, DESZOEKE, HALPERN, and NIILER, 1981) have been observed. Further studies are needed to determine the effectiveness of these nonlinear interactions in removing inertial energy from the surface layer.

Another mechanism for removing inertial energy was proposed by BELL (1978). Undulations in the base of the mixed layer associated with turbulent eddies are advected by horizontally homogeneous inertial oscillations. These motions disturb the underlying thermocline, and generate internal waves through nonlinear interactions. The transport of momentum by the radiating waves results in a drag force on the inertial currents. This mechanism may contribute to the dissipation of surface layer inertial energy, but so far there is no experimental evidence for it.

In the present study we develop a linear model of vertical dispersion of near-inertial internal waves. The basic mechanism is that a surface mixing layer is driven by a time dependent, spatially varying wind stress. Convergence of near-inertial currents leads to Ekman suction (vertical velocity field) at the base of the surface layer. The Ekman suction then generates internal waves which propagate downward into a stratified interior. The vertical energy flux due to these waves acts as a radiational damping mechanism on the near-inertial surface currents.

Energy transport is proportional to, and in the same direction as, the group velocity. For near-inertial internal waves, the group velocity vector is directed at a very shallow angle with respect to a horizontal plane. The vertical component of group velocity increases with increasing stratification and horizontal wavenumber. The objective of this study is to determine, for realistic environmental conditions, whether the stratification is sufficiently strong and the horizontal wavelength of an imposed wind field is sufficiently short to explain the rapid decay of inertial oscillations.

The plan for this report is as follows. In Section 1.2 we present the basic model equations of motion. In Section 2 we perform a Fourier series expansion in the x-direction, and describe the method of solution. Section 3 presents a validation of the model against an analytic solution for the simple special case of an unstratified diffusive fluid. The dispersion of near inertial waves into a uniformly stratified fluid is described in Section 4. The influence of stratification on the dissipation of surface layer inertial oscillations is also discussed. In Section 5 we consider the case of a more realistic nonuniformly stratified fluid. We compare these results with shallow-water current meter observations. In Section 6 we summarize the results of our work during FY81 and FY82, and outline our recommendations for future work.

1.2 EQUATIONS

KROLL (1975) developed a wave packet propagation model, in which the Ekman suction at the base of a viscous boundary layer drives an inviscid stratified interior. The boundary layer is decoupled from the interior, and the super-inertial frequency differential of the interior forcing (the difference between the Ekman suction frequency and the local inertial frequency) is prescribed to be constant. For our purposes, this model must be extended. We do not decouple the boundary layer from the interior, because we wish to study the mutual interaction between the two layers. Also, we do not specify a single frequency component, but treat all frequency components of the forcing simultaneously.

In certain respects, the model we develop is similar to that of KRAUSS (1978, 1979, 1981). Krauss' model

is based on the linearized hydrodynamical equations of motion in a viscous, Boussinesq, rotating fluid. Internal gravity waves are generated in a flat bottomed channel of finite width and infinite length. The major change we make to KRAUSS' model is the addition of porous damping in a thin layer just above the bottom boundary of the computational domain. The purpose of this porous region is to absorb internal waves, and prevent them from reflecting off the bottom boundary. We also extend the interpretation of the system to the open ocean.

We also make some other minor changes to KRAUSS' model equations. We ignore the horizontal eddy diffusion terms, and since we are concerned with near-inertial motions, we assume the hydrostatic approximation. We choose an orthogonal coordinate system (x,y,z), with z directed positive upwards. Table 1.1 is a list of the variables. For a complete development of the model equations, we refer the reader to RUBENSTEIN (1980). The equations are as follows:

$$\frac{\partial u}{\partial t} - fv = -\frac{\partial p}{\partial x} + \frac{\partial}{\partial z}\left(\mu \frac{\partial u}{\partial z}\right) - \sigma u, \tag{1.1}$$

$$\frac{\partial v}{\partial t} + fu = -\frac{\partial p}{\partial y} + \frac{\partial}{\partial z}\left(\mu \frac{\partial v}{\partial z}\right) - \sigma v, \tag{1.2}$$

$$0 = -\frac{\partial p}{\partial z} + b, \tag{1.3}$$

$$\frac{\partial b}{\partial t} + N^2 w = 0, \tag{1.4}$$

$$\frac{\partial u}{\partial x} + \frac{\partial v}{\partial y} + \frac{\partial w}{\partial z} = 0. \tag{1.5}$$

Table 1.1
DEFINITIONS OF VARIABLES

x, y, z	Right-handed coordinate system, z positive up, z = 0 at bottom, D at surface.
u, v, w	Velocity components
t	Time
p	p'/ρ_o, where p' is pressure fluctuation from a reference state, and ρ_o is a representative value of density.
μ	Eddy diffusivity, a function of z only
N	Vaisala frequency; $N^2 = -\left(\frac{g}{\rho_o}\frac{d\rho_r}{dz}\right)$, where $\rho_r(z)$ is a reference state of density.
b	Buoyancy; $-\rho' g/\rho_o$, where ρ' is density fluctuation from a reference state.
f	Inertial frequency = $2\Omega\sin$(latitude)
σ	Porous damping coefficient; zero except in a thin region near the bottom boundary.

Here, the terms σu and σv are the damping terms, which we discuss further in Section 2.1. The $N(z)$ and $\mu(z)$ distributions are constant in time, horizontally homogeneous, and represent statistical averages. In Section 4, we specify that they not overlap one another. If there were significant turbulence just below the mixed layer, the seasonal thermocline would erode further and entrain additional fluid into the mixed layer. Therefore we have neglected the buoyancy eddy diffusivity term, and the processes which maintain the mean buoyancy profile against diffusion. The boundary conditions are as follows:

$$w = 0 \text{ at } z = 0, D, \tag{1.6}$$

$$\frac{\partial u}{\partial z} = \frac{\partial v}{\partial z} = 0 \text{ at } z = 0, \tag{1.7}$$

$$\mu \left(\frac{\partial u}{\partial z} , \frac{\partial v}{\partial z} \right) = - \underline{\tau}(x,y,t) \text{ at } z = D,$$

The surface stress vector $\underline{\tau}(x,y,t)$ is a prescribed function which drives the system. Equation (1.6) states that velocities normal to the top and bottom boundary surfaces should vanish. Equation (1.7) prescribes that the stress, and therefore the shear at the bottom should be zero. This boundary condition allows slippage at the bottom of the computational domain which, after all, is an artifice of the model.

Section 2
SOLUTION APPROACH

2.1 TRANSFORMED EQUATIONS

In this section we present the model equations, and develop their method of solution. We assume that the wind-induced surface stress vector can be described as a Fourier transform

$$\underline{\tau}(x,y,t) = \int_{-\infty}^{\infty} d\underline{k}\, \exp(i\underline{k}\cdot\underline{x})\, \underline{\tau}(\underline{k},t) \ . \qquad (2.1)$$

We consider the wind-induced stress associated with a propagating frontal system. We choose the coordinate system so that the x-coordinate is aligned in the direction of propagation of the front. We assume that the front is invariant in the y-direction, normal to the direction of propagation.

As our model equations are linear, the system separates for each wavenumber vector $\underline{k}$. With the above assumptions in mind, each vector $\underline{k}$ is directed in the x-direction, the direction of front propagation. Writing $k = |\underline{k}|$, the general solution is

$$\begin{Bmatrix} u \\ v \\ w \\ p \\ b \end{Bmatrix} (x,z,t) = \int_{-\infty}^{\infty} dk\, \exp(ikx) \begin{Bmatrix} \hat{u} \\ \hat{v} \\ \hat{w}k^2/ik \\ \hat{p}/ik \\ \hat{b}/ik \end{Bmatrix} (k,z,t) \ . \qquad (2.2)$$

Dropping the hats, the equations of motion become

$$\frac{\partial u}{\partial t} - fv = -p + \frac{\partial}{\partial z}(\mu\frac{\partial u}{\partial z}) - \sigma u$$

$$\frac{\partial v}{\partial t} + fu = \frac{\partial}{\partial z}(\mu\frac{\partial v}{\partial z}) - \sigma v$$

$$-\frac{\partial p}{\partial z} + b = 0$$

$$\frac{\partial b}{\partial t} + N^2 k^2 w = 0$$

$$\frac{\partial w}{\partial z} - u = 0 \qquad (2.3a\text{-}e)$$

and the boundary conditions are

$$w = 0 \text{ at } z = 0, D$$

$$\frac{\partial u}{\partial z} = \frac{\partial v}{\partial z} = 0 \text{ at } z = 0$$

$$\mu(\frac{\partial u}{\partial z}, \frac{\partial v}{\partial z}) = \underline{\tau} \text{ at } z = D. \qquad (2.4a\text{-}c)$$

The shape and magnitude of $\sigma(z)$ is crucial to the reduction of bottom reflections. The magnitude of $\sigma(z)$ must be sufficient to absorb wave packets as they propagate downward through the porosity region, reflect off the bottom, and propagate upward again. If the vertical gradient of $\sigma(z)$ is too big, then waves will reflect off the porosity distribution itself, before they are sufficiently damped. We have a great deal of experience using porous damping formulations with another internal waves code, GORWAK (ROBERTS and RUBENSTEIN, 1981). A useful formulation for $\sigma(z)$ is

$$\sigma(z) = A \exp\left[-\sinh(\sinh z/B)\right]. \qquad (2.5)$$

The constant B is a depth scale, and characterizes the thickness of the porosity distribution. The gradient $d\sigma/dz$ decreases with increasing B, so by making B large, we minimize reflections off the porosity distribution. As we increase B we decrease the size of the porosity-free computational domain, so we strike a compromise, and let $B = 0.4D$. Through experimentation, we find that $A \sim f$ is an optimal value which minimizes reflections off the bottom.

2.2 METHOD OF SOLUTION

2.2.1 Finite-Difference Mesh

We choose to solve the equations and boundary conditions (2.3), (2.4) using a finite difference scheme. The scheme is leap frog in time, and staggered and stretched in depth. Figure 2.1 shows a schematic representation of the finite difference mesh. The time-step constraint due to numerical instability of the diffusion terms, namely

$$\delta t < (\delta z)^2/\mu, \qquad (2.6)$$

is very serious. With $\delta z = 100$ cm resolution, and a typical value of eddy diffusivity $\mu = 100$ cm^2/sec, the time step δt must be less than 100 sec. In order to avoid the constraint (2.6), we construct a hybrid implicit scheme, where the diffusion and porosity terms are implicitly formulated. The other terms remain explicit.

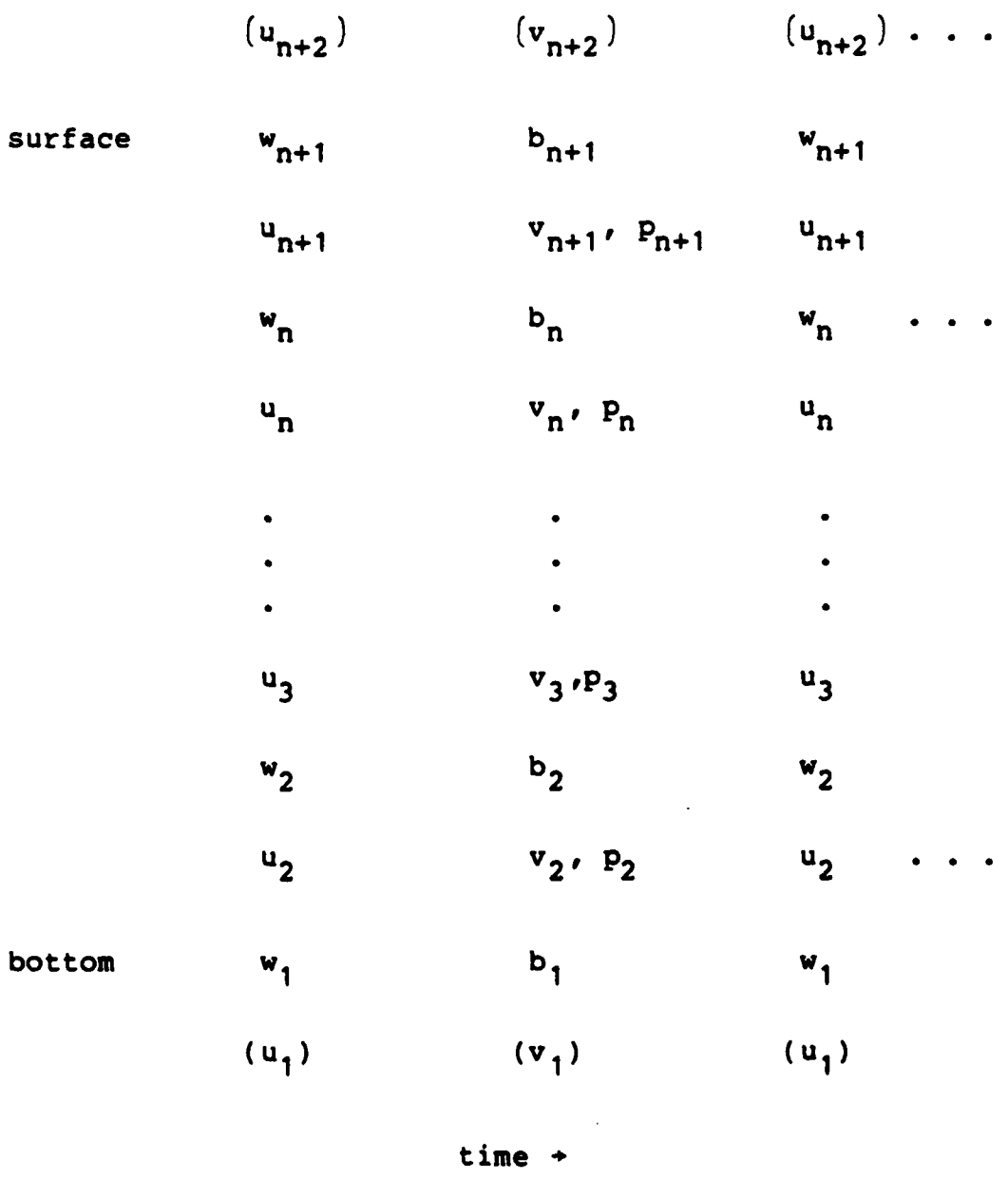

Figure 2.1 Schematic of finite difference mesh. The mesh is staggered in depth and in time. The mesh is divided into n unequal intervals in depth. The variables enclosed in parentheses are outside the domain, and are determined by the boundary conditions.

The depth coordinate is stretched according to the formula

$$j = \frac{n}{\ln(\gamma/(1+\gamma))}\ln\left(\frac{1+\gamma-z/D}{1+\gamma}\right) + 1, \qquad (2.7)$$

where j is an integer or half-integer index, n is the number of mesh intervals, and γ is a stretching parameter. We can solve for z to get

$$z/D = 1 + \gamma - \exp\left[\frac{j-1}{n}\ln(\gamma/(1+\gamma)) + \ln(1+\gamma)\right]. \qquad (2.8)$$

2.2.2 Time-Step Increment

The predictive equations (2.3a), (2.3b), and (2.3d) for u, v, and b are integrated by computing the increments δu, δv, and δb, and accumulating these increments to advance forward to the next time step. For example, we introduce our notation for the v-momentum equation;

$$v^{i+1} = v^i + \delta v, \qquad (2.9)$$

where the superscripts indicate the time step. We write the v-momentum equation in the form

$$\frac{v^{i+1} - v^i}{\delta t} = -fu^i + \partial_z \mu \partial_z (v^i + \theta \delta v) - \sigma(v^i + \theta \delta v), \qquad (2.10)$$

where θ is a parameter which specifies the degree of implicitness. For all cases discussed in this report, we let $\theta = 1/2$. Rearranging, (2.10) becomes

$$\left(\frac{1}{\delta t} + \theta\sigma - \theta\partial_z \mu \partial_z\right)\delta v = -fu^i + \partial_z \mu \partial_z v^i - \sigma v^i. \qquad (2.11)$$

The expression in parentheses on the left hand side may be represented by a tridiagonal matrix. We solve for δv using a vectorized tridiagonal solving routine written by J. Boris for use on the Texas Instruments Advanced Scientific Computer at the Naval Research Laboratory.

2.2.3 Momentum Transport Constraint

We can integrate the hydrostatic balance equation (2.3c) to obtain the pressure to within a constant, α;

$$p = \int_0^z b\,dz + \alpha\,. \tag{2.12}$$

We split the time-step increment δu into two components,

$$\delta u = \delta\bar{u} + \alpha\delta\tilde{u}, \tag{2.13}$$

where $\delta\bar{u}$ and $\alpha\delta\tilde{u}$ are driven by the two components of (2.12), respectively.

The first component $\delta\bar{u}$ is the solution to the finite difference equation

$$\left(\frac{1}{\delta t} + \theta\sigma - \theta\partial_z\mu\partial_z\right)\delta\bar{u} = fv^i - \int_0^z b\,dz + \partial_z\mu\partial_z u^i - \sigma u^i, \tag{2.14}$$

where the buoyancy integral gives the partial pressure, apart from α. Also, $\delta\bar{u}$ satisfies the inhomogeneous boundary condition at the surface

$$\mu\partial_z(\delta\bar{u}) = \partial\tau_x; \quad z = D, \tag{2.15}$$

and the homogeneous boundary condition at the bottom

$$\mu\partial_z(\delta\bar{u}) = 0; \quad z = 0. \tag{2.16}$$

The second component $\delta\tilde{u}$ is the solution to the equation

$$\left(\frac{1}{\delta t} + \theta\sigma - \theta\partial_z\mu\partial_z\right)\delta\tilde{u} = 1, \tag{2.17}$$

and satifies the homogeneous boundary conditions

$$\mu\partial_z(\delta\tilde{u}) = 0; \quad z = 0,D. \tag{2.18}$$

Note that the expressions in parentheses in (2.11), (2.14) and (2.17) are identical. Also note that (2.17) and (2.18) are independent of time, so we need to solve for $\delta\tilde{u}$ only once. In order to solve for α we impose an additional constraint

$$\int_0^D u\,dz = 0\ , \tag{2.19}$$

obtained by integrating the continuity equation (2.3e) with respect to depth and applying the boundary condition (2.4a).

2.2.4 Solution Algorithm

In this section we outline the steps of the solution algorithm.

1. Initialize u, v, b, and p to zero. Multiply N^2 by the chosen k^2 value.

2. Using (2.17) and (2.18), solve for $\delta\tilde{u}$.

3. Integrate the hydrostatic relation (2.3c) to obtain the (partial) pressure;

$$p(z) = \int_0^z b \, dz. \tag{2.20}$$

4. Solve (2.11) for δv, subject to the boundary conditions (2.4). Use (2.9) to get the new updated value of v.

5. Solve (2.14) - (2.16) for $\delta\bar{u}$.

6. Perform a preliminary update on u to get an intermediate value;

$$u^* = u + \delta\bar{u}. \tag{2.21}$$

7. Use the constraint (2.19) to solve for α;

$$\alpha = \frac{-\int_0^D u^* \, dz}{\int_0^D \delta\tilde{u} \, dz}. \tag{2.22}$$

Note that the denominator in (2.22) is constant in time.

8. Perform an update on u;

$$u = u^* + \alpha\delta\tilde{u}. \tag{2.23}$$

9. Integrate the continuity equation (2.3e) to obtain w;

$$w(z) = \int_0^z u \, dz. \tag{2.24}$$

10. Perform an update on b;

$$b_{new} = b_{old} - \delta t \, k^2 \, N^2 w \tag{2.25}$$

11. Repeat steps (3) - (10) until the desired integration time is reached.

Section 3
CODE VALIDATION

In this section we validate the numerical code for the special case of an unstratified fluid, where an analytic solution is available. The equations can be simplified if we define a new time variable $t' = tf$ and a new eddy diffusivity $\mu' = \mu f^{-1}$. This allows us to eliminate the Coriolis parameter f from the equations. We set $N = \sigma = 0$ in (2.3), and drop the primes, leaving us with the equations

$$\partial_t u - v = \partial_z(\mu \partial_z u) ,$$

$$\partial_t v + u = \partial_z(\mu \partial_z v) ,$$

$$\partial_z w - k^2 u = 0 . \qquad (3.1a\text{-}c)$$

We examine the special case where the eddy diffusivity is constant, $\mu = 10^{-3}$. Note that since stratification has been set to zero, the buoyancy and pressure fluctuations have left the problem. The continuity equation (3.1c) relates w and u, but w is a passive variable, so it can be safely ignored. We let $U = u + iv$, so that (3.1a,b) can be combined to read

$$(\partial_t + i - \mu\partial_{zz})U = 0 . \qquad (3.2)$$

For boundary conditions we let

$$\mu\partial_z U = \tau \qquad z = 0, \qquad (3.3)$$

$$U \to 0 \qquad z \to -\infty , \qquad (3.4)$$

where τ is the complex surface stress.

From GONELLA (1971), the general solution starting from an initial velocity $U_o(z) = U(z,0)$ is

$$U(z,t) = U_1(z,t) \underset{(z)}{*} U_o(z) + U_1(z,t) \underset{(t)}{*} 2\tau(t), \quad (3.5)$$

where

$$U_1(z,t) = Y(t) \frac{e^{-it}}{(4\pi\mu t)^{1/2}} \exp(-z^2/4\mu t) , \quad (3.6)$$

and $Y(t)$ is the Heaviside step function. The asterisks denote convolution operations, the first with respect to z and the second with respect to t.

We consider the special case where the initial velocity is zero, and the x-component of surface stress is impulsive;

$$U_o(z) = 0 , \quad (3.7)$$

$$\tau(t) = \delta(t) \quad (3.8)$$

Substituting (3.6)-(3.8) into (3.5) we get $U(z,t) = 2U_1(z,t)$. At the surface $z = 0$, the solution is

$$U(0,t) = \frac{Y(t)\, e^{-it}}{(\pi\mu t)^{1/2}} . \quad (3.9)$$

The solution describes inertial oscillations with an amplitude which decays as $t^{-1/2}$. The reason for this decay is the diffusion of momentum through a surface layer whose thickness grows as $t^{1/2}$.

We integrated (3.1) using the numerical code for 8 inertial periods. The number of mesh intervals was $n = 90$, and the stretching parameter in (2.7) was $\gamma = 0.1$, which corresponds to mesh spacing exactly eleven times finer at $z = 1$ than at $z = 0$. The time step δt was $\pi/32$. In Figure 3.1, the first 2.5 inertial periods of the numerical solution are compared with the analytic solution (3.9). Because the depth average of u in the numerical model is constrained to be zero, and the bottom boundary condition allows slip, we subtracted the bottom velocity from the surface velocity before displaying the results. The numerical solution has been corrected for the lag which occurs because the surface stress is not a true impulse, but is applied over the duration of the first time step. With these corrections, the comparison is excellent.

Figure 3.2 gives the reader a good feel for the overall behavior of the solution. In this figure, the v-component of velocity, computed numerically, is plotted as a function of z and t. The first 3.75 inertial periods are shown. One can clearly see the inertial oscillations, which are strongest in the surface layer. The depth of the surface layer is delineated by the gently sloped solid line which represents zero amplitude. The depth of the surface layer increases as $t^{1/2}$ for small t. For large t, the depth asymptotically approaches $z = 1/2$, for the reasons described above, in the previous paragraph.

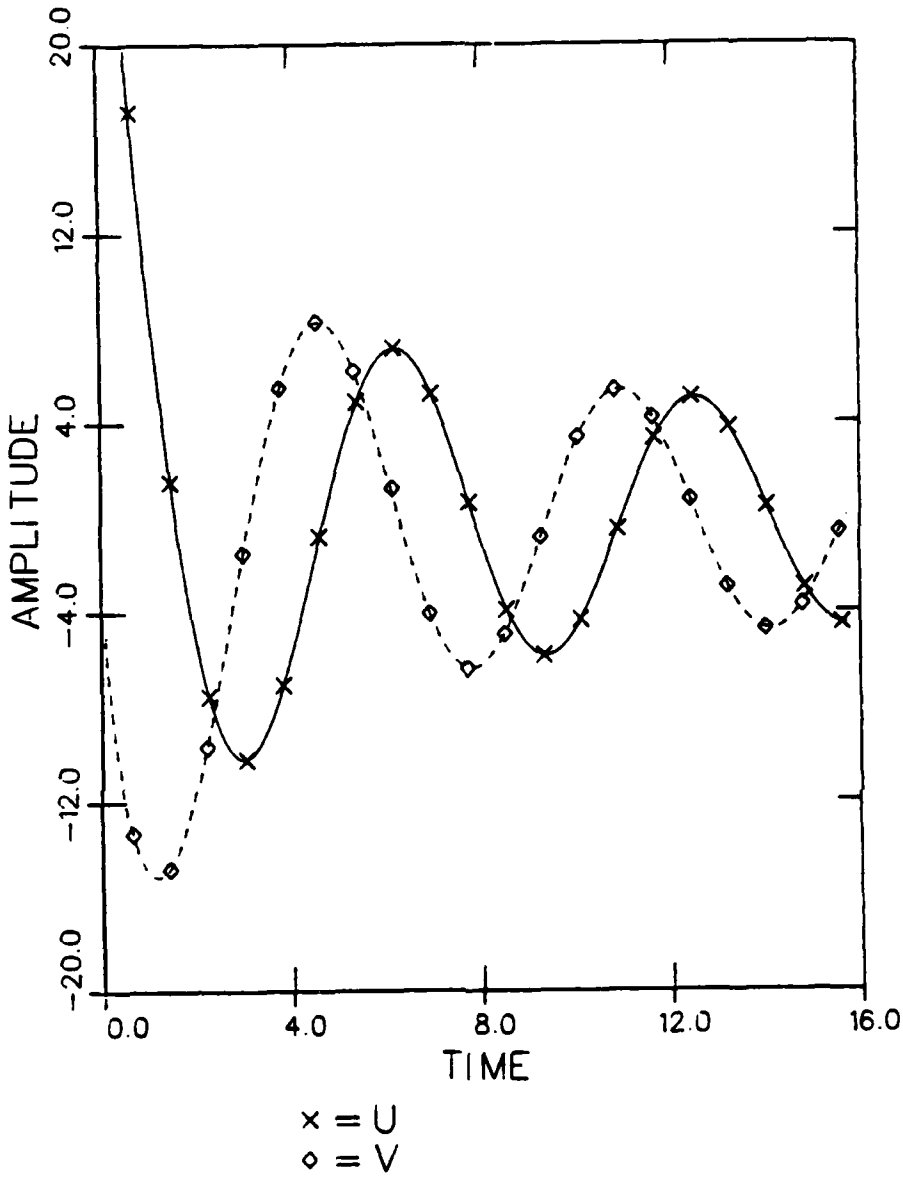

Fig. 3.1 Comparison between analytic solution at surface (solid; u component and dashed; v component curves) and numerical solution (crosses and diamonds). An impulsive wind stress is applied to the surface of an unstratified, rotating fluid at time t = 0.

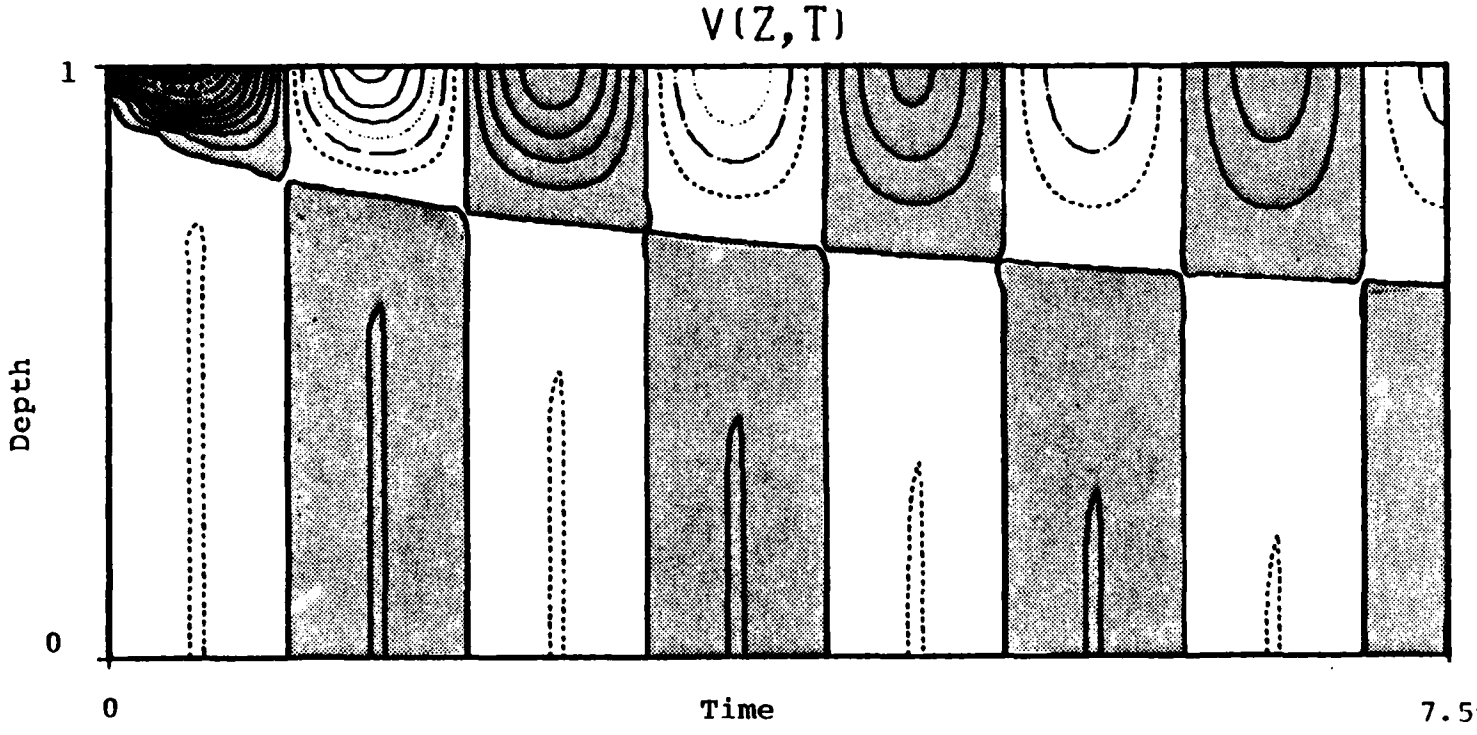

Fig. 3.2 V-component of velocity, in response to an initial impulsive surface stress at t = 0, for purely diffusive, unstratified case. Shaded and unshaded regions are positive and negative, respectively.

Section 4
INERTIAL WAVES IN A SURFACE LAYER OVERLYING A UNIFORMLY STRATIFIED THERMOCLINE

In this section we examine the dispersion of near-inertial internal waves in a uniformly stratified thermocline, and their resultant decay in the surface layer. We consider here only impulsive surface stress forcing. This rather extreme simplification of real wind events allows us to separate out the effects of phase interference of surface layer inertial oscillations, which accompany wind events of finite duration.

We examine the idealized case where both stratification and eddy diffusivity are step functions in depth;

$$N(z) = \begin{cases} N_o & 0 \leq z < h \\ 0 & h \leq z \leq D \end{cases} \tag{4.1}$$

$$\mu(z) = \begin{cases} 0 & 0 \leq z < h \\ \mu_o & h \leq z \leq D \, . \end{cases} \tag{4.2}$$

The depth D-h is the mixed layer depth. The eddy diffusivity μ_o allows momentum to diffuse throughout the unstratified region $h \leq z \leq D$. The $N(z)$ and $\mu(z)$ distributions do not overlap. Momentum cannot diffuse below $z < h$, but must be transported via internal waves through the stratified

interior. Table 4.1 lists the parameters for all of the cases discussed in Section 4.

In all cases in this section and in Section 5, the time step increment was 1/64 of an inertial period, or 982 sec. The surface stress driving function was an impulse in the y-direction. This impulse lasted for the duration of the first time step, and was then turned off. The reason for applying an impulse is that we wanted to study the effects of vertical dispersion in isolation from other factors. If we had used a realistic wind event, lasting an appreciable fraction of an inertial period, then phase interference effects would become important.

For a similar reason, we chose values of eddy diffusivity which are probably unrealistically large. The role of diffusivity is simply to redistribute momentum through the surface layer. Tests show that the depth-averaged energy in the surface layer and in the stratified region is quite insensitive to the value of μ_o. The advantage to using a large diffusivity is that the momentum redistribution can occur quickly. Therefore, the dissipation of surface layer inertial oscillations due to internal wave dispersion is separated from that due to diffusion.

The magnitude of the surface stress, applied during its initial impulse, was 0.08 $m^2 s^{-2}$. If this stress were distributed over a realistic "frontal passage time", say, 1/4 of an inertial period (about 4.4 hours), then this stress impulse is equivalent to a distributed magnitude of 5.3×10^{-4} $m^2 s^{-2}$. Therefore, the applied surface stress is equivalent to that due to a sudden wind event lasting 4.4 hours, and having a magnitude of 19 ms^{-1} (about 37 kt).

Table 4.1
Parameters for Cases in Section 4

Case	$N_o k (s^{-1} m^{-1})$	Mixed Layer Depth d(m)	$\mu_o (m^2 s^{-1})$	Porosity
1	1.25×10^{-6}	20	0.02	Yes
2	1.25×10^{-6}	20	0.02	No
3	1.25×10^{-6}	80	0.08	Yes
4	0	20	0.02	No
5	3.125×10^{-7}	20	0.02	Yes
6	6.25×10^{-7}	20	0.02	Yes
7	2.5×10^{-6}	20	0.02	Yes

4.1 EFFECTS OF BOTTOM POROSITY

The principal effect of bottom porosity is to minimize reflections of internal waves off the bottom boundary. In order to demonstrate this effect we performed two model simulations, Case 1 with porosity A = 1.5×10^{-4} s^{-1}, B = 320 m in equation (2.5)) and Case 2 without porosity. The values of $N_o k$, d = D-h, and μ_o in (4.1) and (4.2) were 1.25×10^{-6} $s^{-1}m^{-1}$, 20 m, and 0.02 $m^2 s^{-1}$, respectively. The computational bottom depth D was 800 m, the horizontal wavelength was 100 km, and the Vaisala frequency was 5.7 cph.

After integrating for 16 inertial periods, we computed the Fourier transforms of the v-component of surface velocity, shown in Figure 4.1. The simulations were nearly identical for low frequencies $\omega < f$. Both simulations show a strong resonant spectral peak at $\omega = f$. Above f, the porous simulation spectrum decays monotonically, while the porosity-free case has a series of spectral peaks. We can understand these peaks if we consider the dimensional dispersion relation in a rotating hydrostatic fluid;

$$\omega^2 = f^2 + \frac{k^2 N^2}{\ell^2} , \qquad (4.3)$$

where ω is angular frequency, and k and ℓ are the horizontal and vertical components of the wavenumber vector. In terms of the Vaisala frequency N_o, the dispersion relation for the j'th vertical mode is

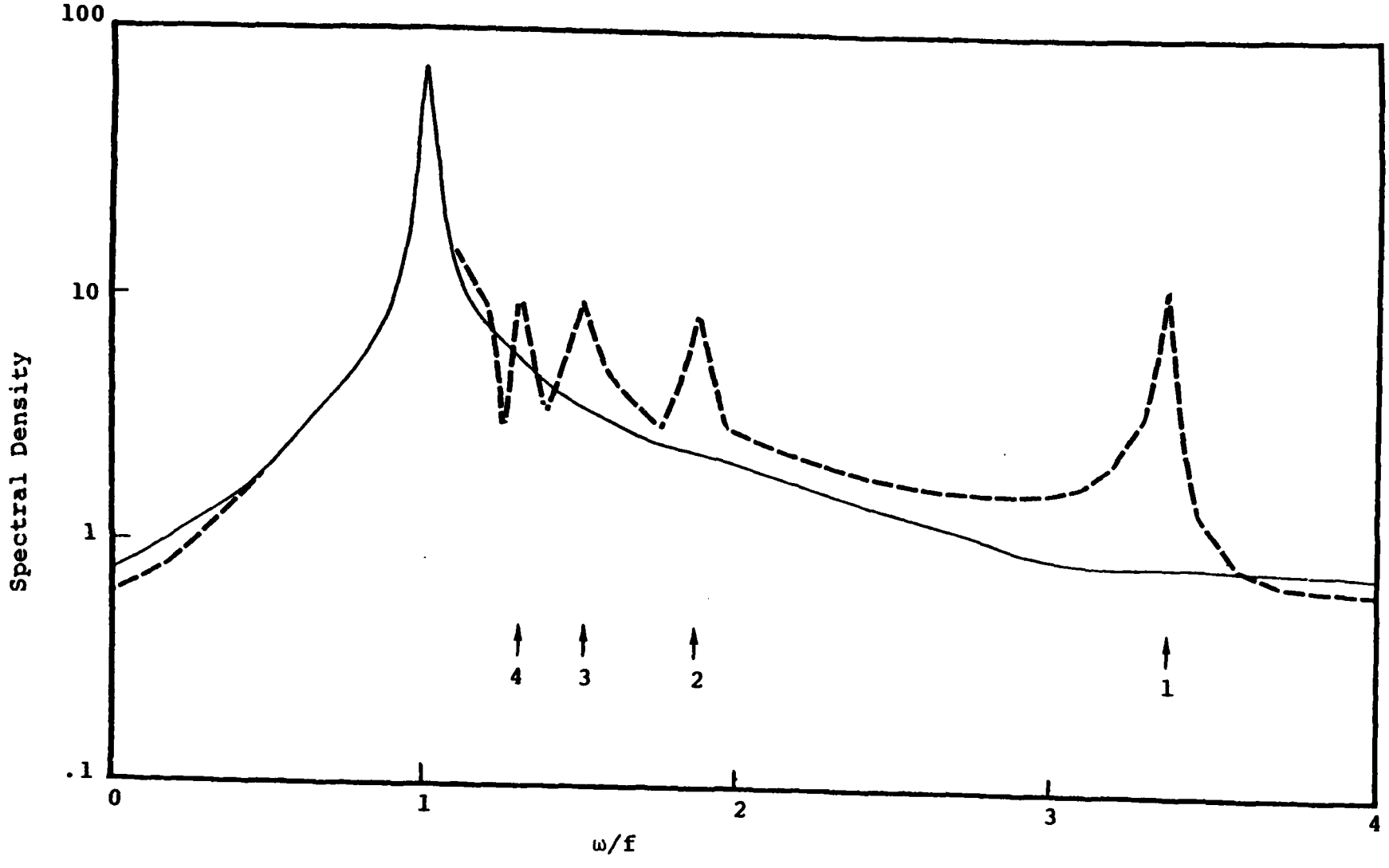

Figure 4.1 Spectral Density of v-component of surface velocity for Case 1 (bottom porosity, solid curve) and Case 2 (no bottom porosity, dashed curve). Frequency axis is normalized in terms of the inertial frequency. Arrows point to the first four vertical mode resonances.

$$\omega_j^2 = f^2 + (N_o kD/j\pi)^2 \ . \qquad (4.4)$$

The normalized frequencies of the lowest four modes for Case 2, with $N_o kD = 10^{-3}$ s^{-1}, are $\omega_j/f = 3.34, 1.88, 1.46, 1.28$; $j = 1, 2, 3, 4$. These frequencies correspond to the four spectral peaks in Figure 4.1.

Thus, we see that the bottom porosity distribution effectively eliminated reflections from the bottom boundary, and prevented the establishment of vertical modes of internal waves. RUBENSTEIN (1981, 1982) examined the porous-free case in detail.

4.2 VERTICAL DISPERSION

In this subsection we examine the vertical dispersion of internal waves in greater detail. We include a bottom porosity distribution in order to minimize bottom reflections.

Figure 4.2 shows the response of the v-component of velocity to a surface stress function applied impulsively at time $t = 0$ in the x-direction, for Case 3. The values of $N_o k$, d, and μ_o in (4.1) and (4.2) are 1.25×10^{-6} $s^{-1}m^{-1}$, 80 m, and 0.08 $m^2 s^{-1}$, respectively. The displayed z domain is unstretched, and ranges from the surface down to a depth of 520 m. Below that depth the solution is not shown, because of the porous damping layer there. The time axis range from $t = 0$ to $t = 7.5\pi/f$, or 3.75 inertial periods.

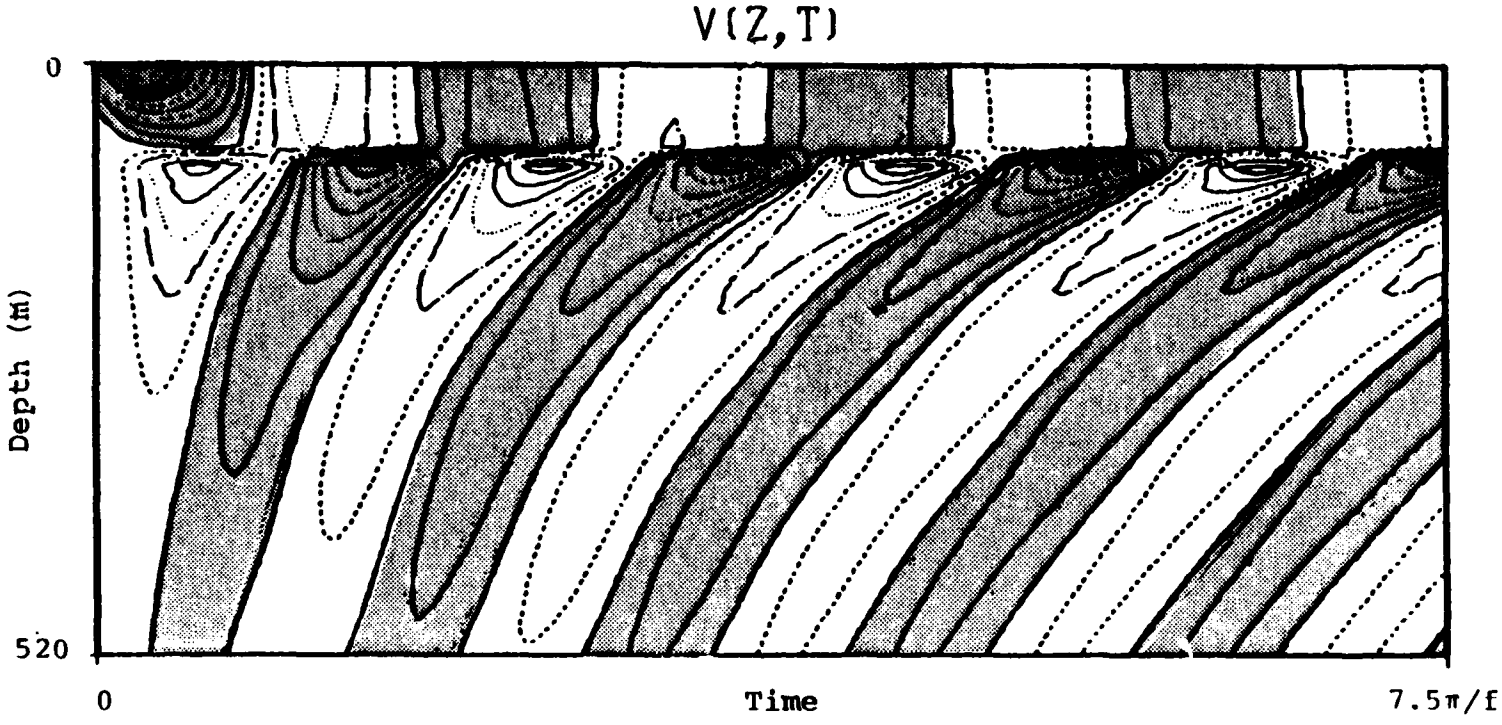

Figure 4.2 V-component of velocity, response to an initial impulsive surface stress at t=0, Case 3. Shaded and unshaded regions are positive and negative. Contour intervals are plotted every 1 cm/sec.

Within half an inertial period after $t = 0$, momentum becomes fairly well diffused through the surface layer, and within a full inertial period ($t = 2\pi/f$), the shear in the surface layer approaches zero. Inertial oscillations are very strong in the surface layer, and the strength slowly decays in time. Meanwhile, internal waves propagate into the stratified interior. From (4.3) we obtain the vertical component of group velocity $c_z = \partial\omega/\partial\ell$;

$$c_z = \frac{k^2N^2}{\omega\ell^3} \quad . \tag{4.5}$$

As the Fourier transform of a delta function is a constant, the initial wind impulse transmits all frequencies equally to the fluid. From (4.3), the highest frequencies are associated with the smallest ℓ. For $\omega >> f$, the vertical group velocity is approximately $c_z \sim kN/\ell^2$. Thus the internal wave components with the smallest ℓ and the largest ω are able to propagate downwards most rapidly, away from the surface. After these waves propagate away, the upper-thermocline region is left with waves with near-inertial frequencies $\omega \gtrsim f$. These waves propagate vertically much more slowly.

In the upper thermocline the vertical phase velocity ω/ℓ, according to our argument above, should decrease with time. In Figure 4.2 shaded and unshaded areas correspond to regions of positive and negative v-component of velocity, and therefore are bands of constant phase. As time progresses these bands slope progressively closer to the

horizontal. This result confirms our expectation that vertical phase velocity decreases with time, and so too does vertical group velocity.

Another feature of interest is the velocity maximum which develops at the top of the stratified interior region. Strong vertical shears develop just above this velocity maximum. For convenience, let us say that at some instant in time, a particular vertical wavelength component Λ_o is dominant in the upper thermocline. Longer wavelength components $\Lambda > \Lambda_o$ have already had time to propagate away. Shorter components $\Lambda \leq \Lambda_o$ are in phase at the density interface and constructively interfere just below the density interface, resulting in a velocity maximum there. As depth below the interface increases, the different components begin to interfere destructively. At some later time the Λ_o component will have propagated away, leaving some shorter dominant component. Hence the vertical extent of the velocity maximum becomes progressively thinner with time. However, the amplitude of this feature does not significantly decay over the course of simulation. After 16 inertial periods, the velocity maximum decreases in strength by only 25%.

4.3 ENERGY PARTITION

We have examined the energy balance in the surface layer and in the stratified region immediately below. Figure 4.3 shows the depth-averaged and time-averaged (over 1/2 cycle) kinetic energy and potential energy in the ranges $0.975 \leq z/D \leq 1.0$ (surface layer) and $0.95 \leq z/D \leq 0.975$ (upper stratified region) for Case 1. Kinetic energy density is given by $\rho|u|^2/2$, and potential energy density is

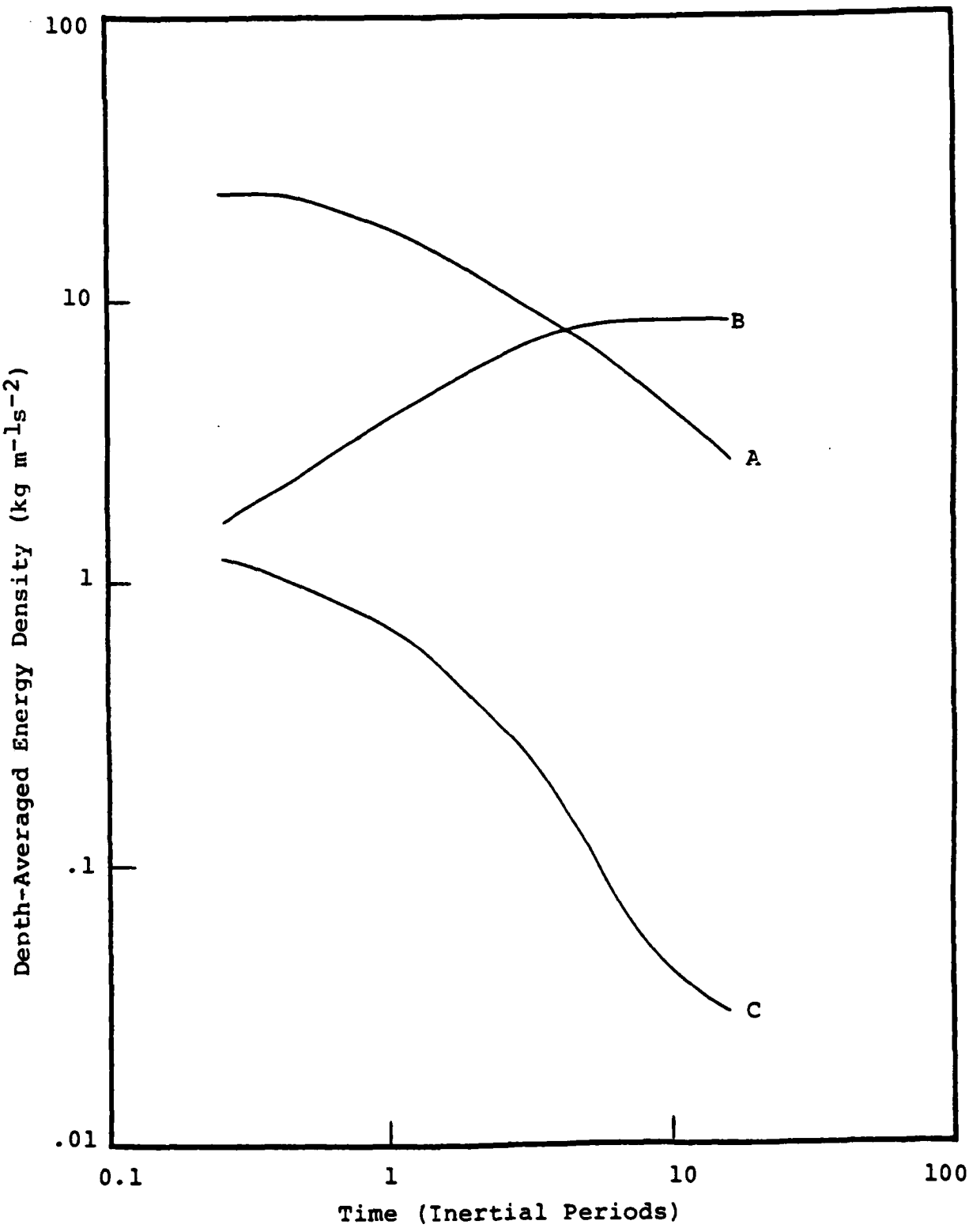

Figure 4.3 Depth-Averaged kinetic energy in surface layer (A), in upper stratified region (B), and potential energy in upper stratified region (C), for Case 1.

$\rho b^2/2N^2$, where ρ is mass density and b is buoyancy. Since the surface layer is unstratified, the potential energy there is zero. Also, since the vertical length scale D is much smaller than the horizontal wavelength $\lambda = 2\pi/k$, the contribution of vertical velocity to the kinetic energy is negligible.

A statement of energy conservation is written

$$\partial_t \left[\tfrac{1}{2}\rho(|\mathbf{u}|^2 + b^2/N^2)\right] + \nabla\cdot(p\mathbf{u}) = 0. \qquad (4.6)$$

In the absence of energy flux pu, kinetic energy can only be gained (or lost) by transforming from (or into) potential energy. Since a fluid particle's buoyancy magnitude $|b|$ has two maxima and minima per wave cycle, kinetic energy also has two maxima and minima per cycle. For this reason the curves in Figure 4.3 represent averages over 1/2-inertial cycles. In the remainder of this section, we represent this time-average operation by a set of angled brackets.

In the upper stratified region, kinetic energy is greater than the potential energy. From LEBLOND and MYSAK (1978), this ratio for a single-frequency plane wave is

$$\frac{\langle E_p\rangle}{\langle E_k\rangle} = \frac{N^2(\omega^2-f^2)}{\omega^2(N^2-f^2) + f^2(N^2-\omega^2)} . \qquad (4.7)$$

The brackets denote an average over a complete cycle. Since $N >> \omega >> f$, we can approximate;

$$\frac{\langle E_p\rangle}{\langle E_k\rangle} \approx \frac{\omega^2-f^2}{\omega^2+f^2} . \qquad (4.8)$$

Note that this ratio is independent of N, and becomes zero in the limit $\omega = f$. Inverting (4.8) to solve for ω, we get

$$\omega = f \left(\frac{1+\langle E_p \rangle / \langle E_k \rangle}{1-\langle E_p \rangle / \langle E_k \rangle} \right)^{1/2} \qquad (4.9)$$

If we keep in mind that our numerical solution represents a continuum of frequencies, we might still use (4.9) in conjunction with the results in Figure 4.3 to estimate the dominant frequency present in the upper stratified region. Figure 4.4 shows $(\omega-f)/f$, where ω is the dominant frequency in the depth range $0.95 \leq z/D \leq 0.975$. We see that the frequency differential decays approximately as $t^{-3/2}$. During the time period $1 \leq t(f/2\pi) \leq 5$, the dominant frequency ω decays from 1.2f to 1.015f. This result is consistent with near-surface observations. Over a wide variety of conditions, GONELLA (1971), PERKINS (1972) and KUNDU (1976) observe spectral peaks at frequencies ranging from 1.007f to 1.11f.

It is possible to estimate the dominant vertical component of the group velocity in the upper stratified region. Combining (4.3) and (4.5) we get

$$c_z = \frac{(\omega^2-f^2)^{3/2}}{\omega k N} \quad . \qquad (4.10)$$

We use (4.9) to provide an estimate of the dominant frequency. Figure 4.5 shows c_z as a function of time, in the depth range $0.95 \leq z/D \leq 0.975$. The vertical component of group velocity c_z decays approximately as $t^{-2.4}$.

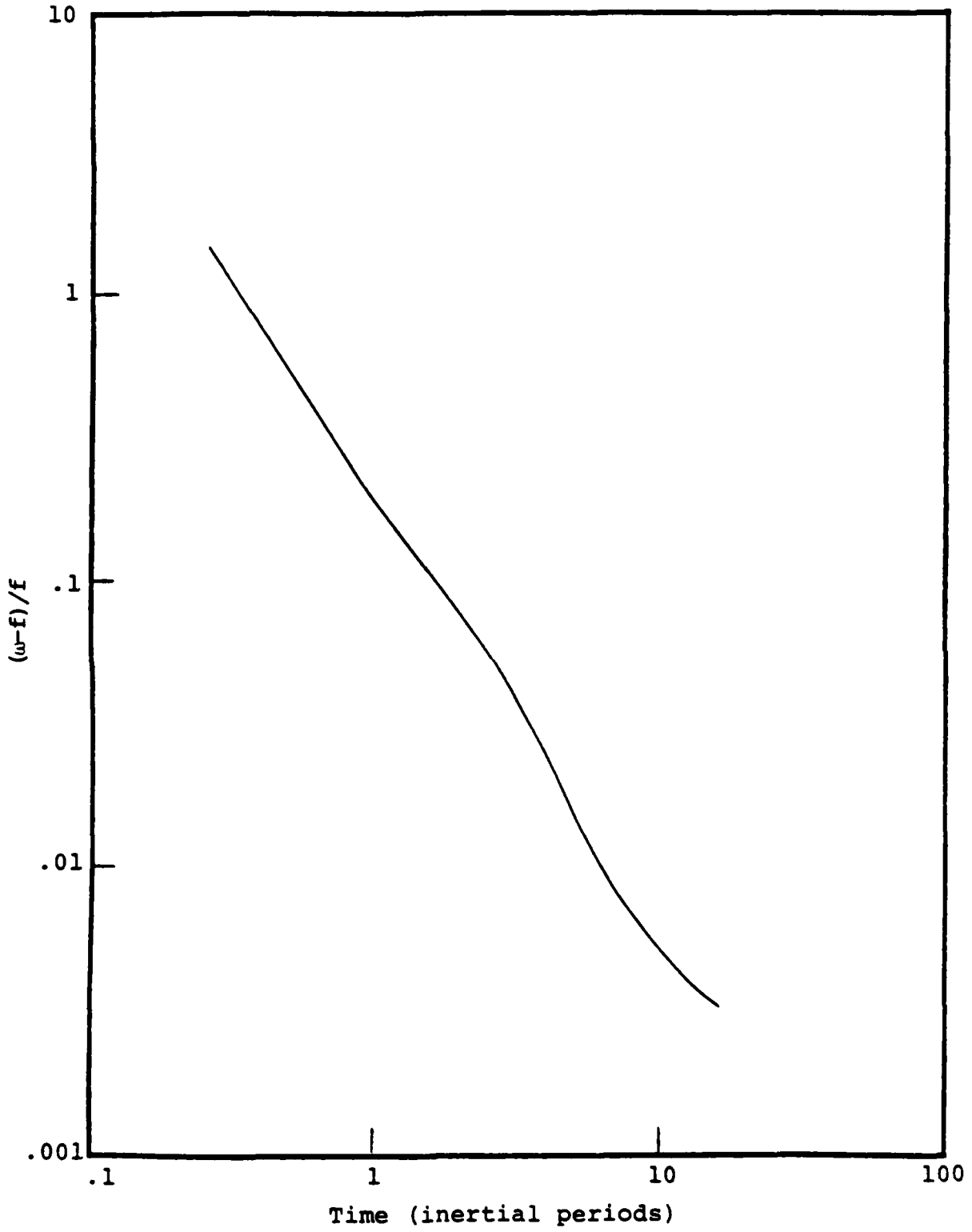

Figure 4.4 Super-inertial frequency differential in the upper stratified region, for Case 1.

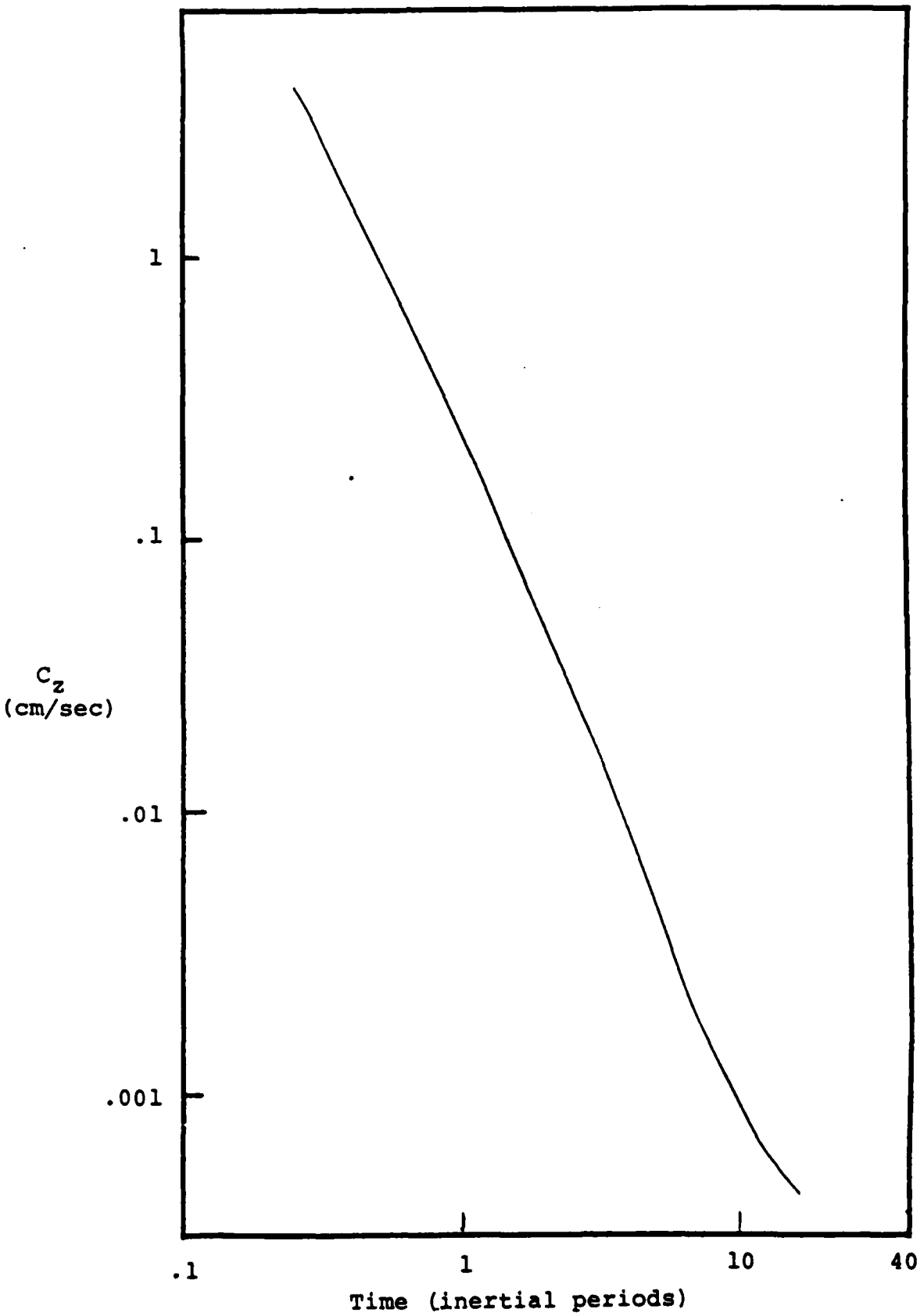

Figure 4.5 Vertical component of group velocity in the upper stratified region, for Case 1.

4.4 STRATIFICATION

One of our primary concerns is the effect of stratification on the dispersion of near-inertial waves. In this section we examine a set of cases, each with a different density stratification, and determine how the dissipation rate of inertial oscillations in the surface layer reacts to varying stratification.

As throughout Section 4, the Vaisala frequency and eddy diffusivity profiles are of the forms given by (4.1) and (4.2). We compared Cases 1, 4, 5, 6, and 7, described in Table 4.1. The values of $N_o k$ were 0, 3.125, 6.25, 12.5, and 25 ($\times 10^{-6}$ $s^{-1}m^{-1}$). The mixed layer depth d was 20 m, and μ_o was 0.02 $m^2 s^{-1}$.

The purpose of Case 4, with $N_o k = 0$, is to describe a base state in which all of the energy is confined to the surface layer. Since the unstratified fluid cannot sustain internal gravity waves, there is no need for bottom porosity. As a result, momentum is conserved--the net momentum is zero--but energy is <u>not</u> conserved. Immediately after the initial surface stress impulse, a sharp momentum gradient is present at the surface. Diffusion redistributes the momentum through the surface layer, and quickly makes the velocity distribution uniform with depth in the surface layer, and the kinetic energy approaches a constant value. In Case 4, the kinetic energy approaches within 1% of its constant final value after time $t = \pi/5f$ (1/10 of an inertial period). Therefore, we can obtain a measure of the dissipation rate of inertial oscillations due to vertical dispersion, by comparing the evolving depth averaged kinetic energy in the surface layer with its "post-diffusion" value at time $t = \pi/5f$.

Figure 4.6 shows the time evolution of depth averaged kinetic energy in the surface layer for Cases 1, 5, 6, and 7. The dissipation rate increases with increasing $N_o k$. For comparison purposes, the e-folding dissipation time scale is a useful quantity, and is tabulated in Table 4.2. These time scale estimates are very approximate. An

Table 4.2

Kinetic Energy e-Folding Dissipation Time Scale, for Mixed Layer Depth d = 20 m

$N_o k$ ($s^{-1}m^{-1}$)	Case	T(inertial periods)
3.125×10^{-7}	5	30
6.25×10^{-7}	6	8
1.25×10^{-6}	1	2.4
2.50×10^{-6}	7	1

approximate empirical formula for the dissipation time scale is

$$T(\text{inertial periods}) \approx (2.175 \times 10^{-6}/N_o k)^{1.7} \quad (4.11)$$

This formula is correct only for the particular value used in Cases 1, 5, 6, and 7 for dimensionless mixed layer depth d = 20 m. Since internal waves do not feel the computational bottom, the only physically meaningful vertical length scale is the mixed layer depth. Therefore, the

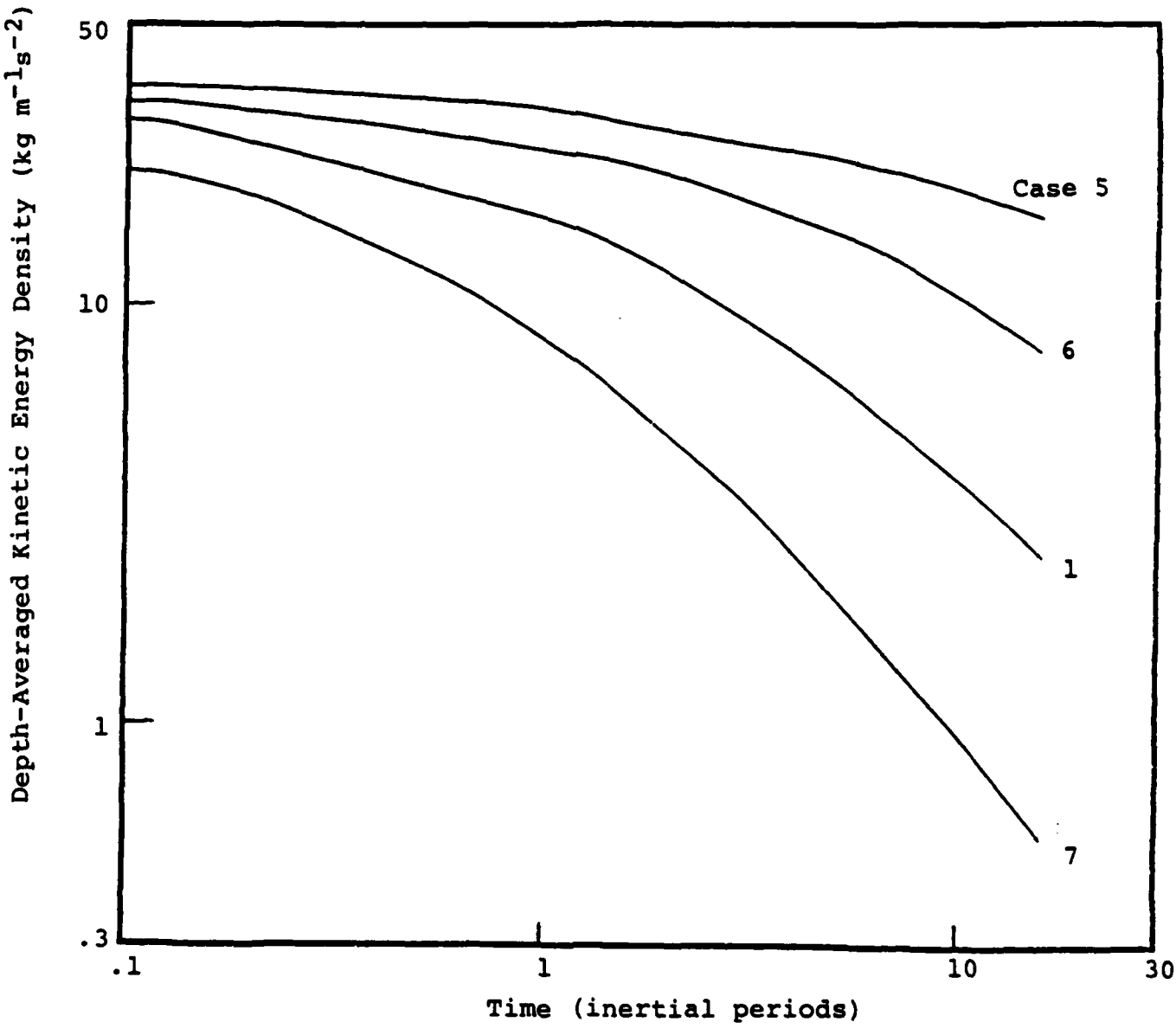

Figure 4.6 Depth-averaged kinetic energy in the surface layer for Cases 5, 6, 1, 7, with $N_o k$ = 3.125 x 10^{-7}, 6.25 x 10^{-7}, 1.25 x 10^{-6}, and 2.5 x 10^{-6} $s^{-1}m^{-1}$, respectively.

relevant dimensionless parameter is Nkd/f, where d is the mixed layer depth. Using this parameter, we can generalize (4.11) to obtain

$$T(\text{days}) \sim \frac{1}{\sin\theta}\left[\frac{\sin\theta\ \lambda(m)}{260\ N\ (cph)d(m)}\right]^{1.7}, \qquad (4.13)$$

where θ is the latitude and $\lambda = 2\pi/k$ is the horizontal wavelength. Table 4.3 shows a tabulation of (4.13), for representative values of λ and N_o. Blank areas in the table are outside the range covered by Cases 1, 5, 6, and 7.

Table 4.3

Kinetic Energy e-Folding Dissipation Time Scale (days), for Latitude $\theta = 40°N$, Mixed Layer Depth d = 20 m.

		λ(km) 25	50	100	200
N (cph) o	2	3.3	10.6		
	4	1.0	3.3	10.6	
	8	0.3	1.0	3.3	10.6
	16		0.3	1.0	3.3

The scale λ is the wavelength associated with an atmospheric front. In a case study of a cold front by HOBBS et al. (1980), the wavelength of the surface wind veering is about 120 km. Squall lines and narrow cold fronts are observed to have associated wavelengths as short as 10 km (CARBONE, 1982; HOBBS and PERSSON, 1982). Direct estimates from observations of inertial oscillations show λ to vary over a wide range. THOMSON and HUGGETT (1981) estimated λ in

fferent regions of and 85-95 km in different regions of
Columbia. SCHOTT f northwest British Columbia. SCHOTT
North Sea to have scillations in the North Sea to have
km.

OLLARD and MILLARD discussed in Section 1.1, POLLARD and MILLARD
the amplitude of the e-folding decay time for the amplitude of
from about 2 to 8 inertial oscillations to range from about 2 to 8
d decay times of 2 (1970) and POLLARD (1980) found decay times of 2
ume that the range respectively. We therefore assume that the range
ecay time for this is representative of the decay time for the
nd therefore the of inertial oscillations, and therefore the
energy e-folding decay time for their kinetic energy is in the
approximate range 1 to 4 days.

in mind, we can with this range of decay times in mind, we can
ch the mixed layer results in Table 4.3 in which the mixed layer
utes significantly m. Vertical dispersion contributes significantly
ertial energy dissipation of surface layer inertial energy for
km is significant the contribution for $\lambda \sim 100$ km is significant
n, $N_o \gtrsim 7$ cph; and sufficiently large stratification, $N_o \gtrsim 7$ cph; and
ficant only for a for $\lambda \sim 200$ km is significant only for a
very strong stratification, $N_o \gtrsim 14$ cph.

Section 5
NONUNIFORM STRATIFICATION

We can extend the results of Section 4 by considering a somewhat more realistic, nonuniform distribution for N(z);

$$N(z') = \begin{cases} 0 & z' \leq 0, \\ N_1 (e/c) z' \exp(-z'/c) & 0 \leq z' \leq c, \\ (N_1/a)\left[(a-1)(e/c) z' \exp(-z'/c) + 1\right] & c \leq z', \end{cases}$$

$$z' = d - z. \qquad (5.1)$$

This profile is shown in Figure 5.1. N(z) is zero in the surface layer (of depth d), has a peak value N_1 at a depth c below the base of the surface layer, and decays asymptotically to N_1/a with large depth. The eddy diffusivity profile is the step function given by (4.2), and is also shown in Figure 5.1. As in Section 4, we again apply a surface stress impulse at time t = 0 in the x-direction. Table 5.1 lists the parameters for all cases discussed in this section.

5.1 SOLUTION OVERVIEW

Figure 5.2 shows the response of the v-component of velocity for Case 1, where no bottom porosity damping is included. Thus, reflections off the bottom of the computational domain are allowed. The z-axis is unstretched, and ranges from 0 to D. The time axis ranges from t = 0 to

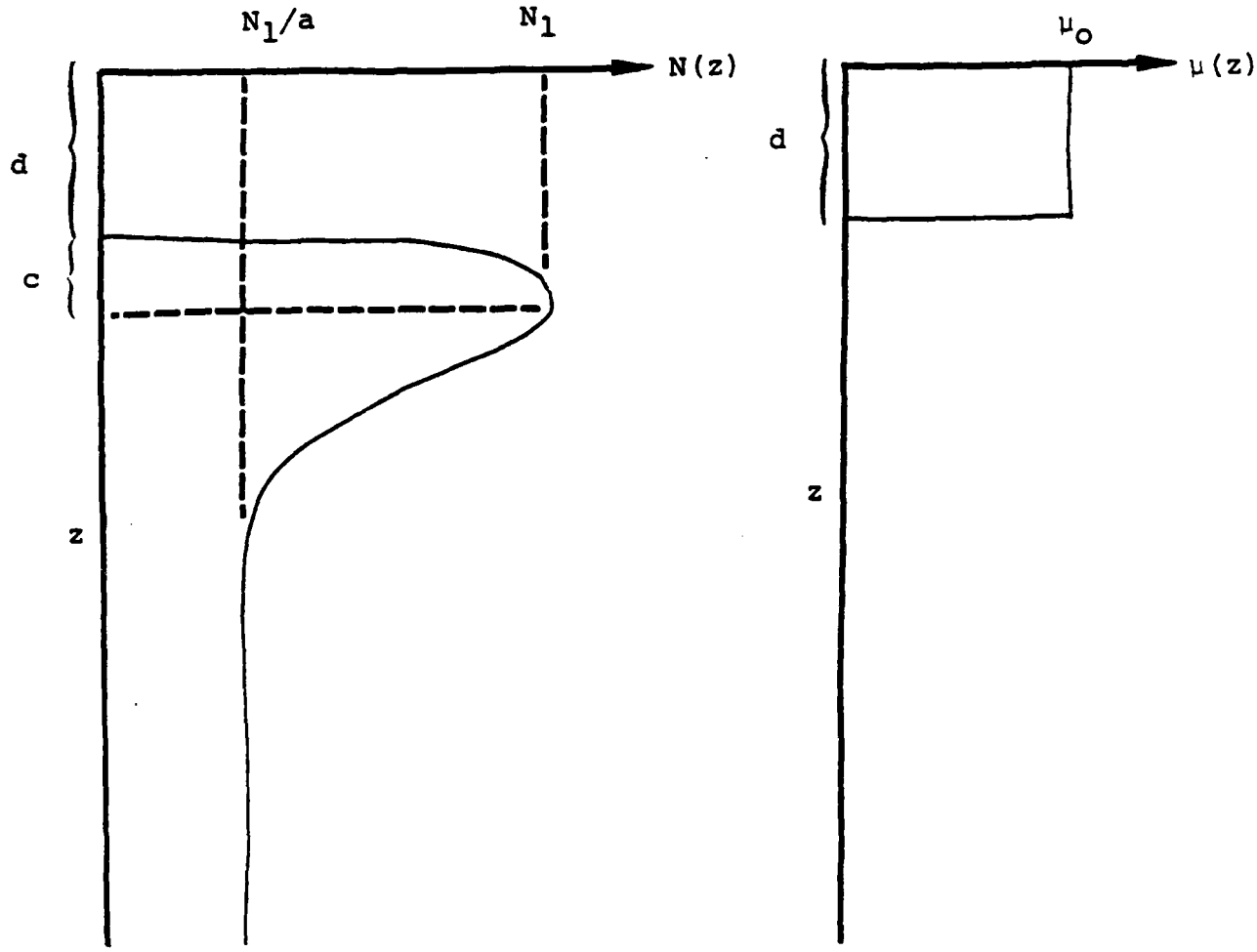

Figure 5.1 Schematic profiles of Vaisala frequency N(z) and eddy diffusivity $\mu(z)$ for cases in Section 5.

Table 5.1
Parameters for Cases in Section 5

Case	$N_1 k$ $(s^{-1}m^{-1})$	d(m)	c(m)	μ_o $(m^2 s^{-1})$	Porosity
1	6.25×10^{-7}	80	40	0.16	No
2	6.25×10^{-7}	80	40	0.16	Yes
3	6.25×10^{-7}	20	10	0.02	Yes
4	1.25×10^{-6}	20	10	0.02	Yes
5	2.5×10^{-6}	20	10	0.02	Yes
6	5×10^{-6}	20	10	0.02	Yes
7	5×10^{-6}	10	2.4	0.02	Yes
8	5×10^{-6}	10	4.8	0.02	Yes
9	5×10^{-6}	10	9.6	0.02	Yes

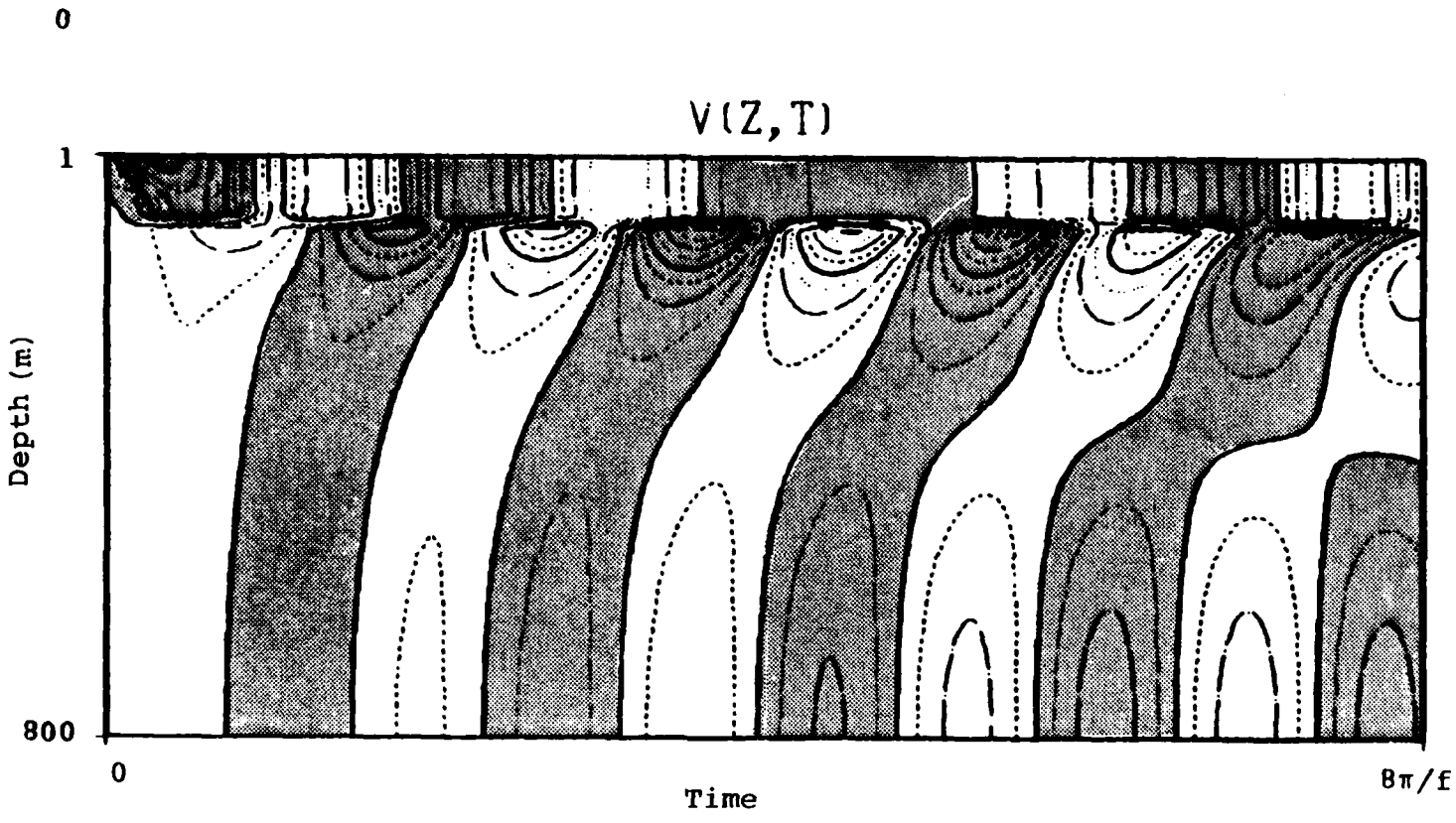

Figure 5.2 Response of v-component of velocity to an initial impulsive surface stress at time t=0, for Case 1. No bottom porosity is used here. Contour intervals are plotted every 1.2 cm/sec. The time axis runs from 0 to 4 inertial periods, or about 3 days.

$8\pi/f$, or 4 inertial periods. Momentum becomes evenly diffused through the surface layer during the first 1/4 inertial period. The flow in the surface layer oscillates at a near-inertial frequency. Internal waves propagate into the stratified region, and a velocity maximum develops just below the surface layer. These features are qualitatively similar to the uniformly stratified case shown in Figure 4.1, but since the stratification in Figure 5.2 is weaker, the vertical phase velocity is greater and the bands of constant phase are more nearly vertical. After time $t = 4\pi/f$ (2 inertial periods), reflections off the bottom boundary become important and generate an interference pattern. We show this solution in order that we can make a comparison with observations in a shallow-bottom sea, in Section 5.3.

In the deep ocean, the ocean bottom has a negligible effect on the propagation of near-inertial waves. Figure 5.3 shows the v-component of velocity for Case 2, where a bottom porosity distribution has been introduced in the approximate range $0 \leq z \leq 0.35D$. The z-axis here ranges from 0.35D to D, (the depth ranges from the surface down to 520 m) in order to avoid overlapping this porosity distribution. Internal waves are absorbed, and thus the model simulates an ocean of infinite depth. The principal difference between Figures 5.2 and 5.3 is that Figure 5.3 lacks the interference pattern in the deeper half of the computational domain, which results from bottom reflections.

5.2 SURFACE LAYER DISSIPATION

Close inspection of Figures 5.2 and 5.3 shows an interesting feature which is absent from the uniformly stratified solution. The amplitude of the surface layer

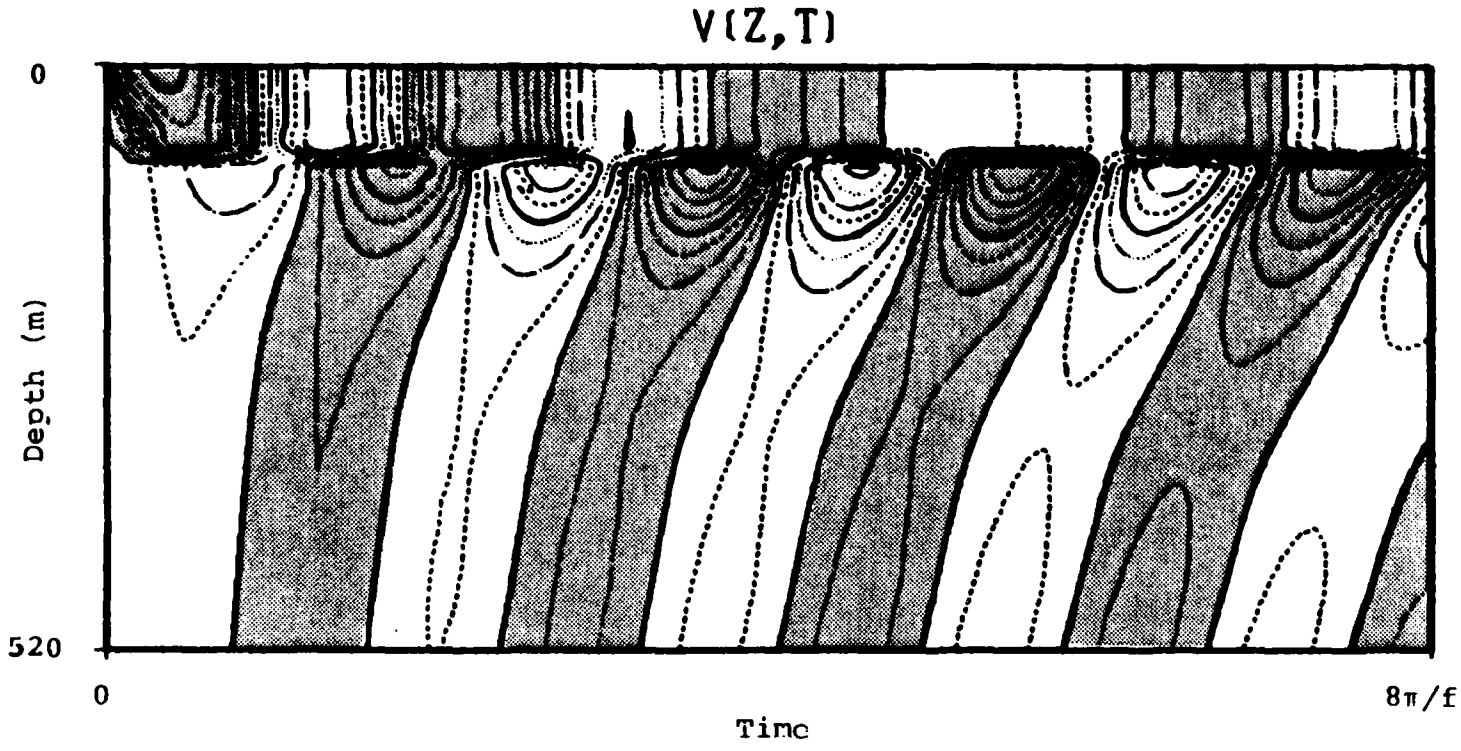

Figure 5.3 Response of v-component of velocity to an initial impulsive surface stress at time t=0, for Case 2. Bottom porosity is used here. Contour intervals are plotted every 1.2 cm/sec.

inertial oscillations, as well as the amplitude of the velocity maximum just below the surface layer are both periodic, and about 180° out of phase from each other. This behavior is analogous to that of two coupled oscillators. This "frequency interference effect" results from the peak in the Vaisala frequency profile, which causes certain internal wave components to resonate and, in a sense, to become partially trapped. Figure 5.4 shows the oscillations of depth-averaged kinetic energy density in the surface layer $0.9 \leq z/D \leq 1.0$ and in the strongly stratified layer $0.8 \leq z/D \leq 0.9$, for Case 2. The period of these oscillations is about 4.6 inertial periods, and remains constant throughout the integration.

Figure 5.5 shows the time evolution of depth averaged kinetic energy density in the surface layer for Cases 3-6. The dissipation rate increases with increasing N_1. The e-folding dissipation time scale is tabulated in Table 5.2. These time scale estimates are very approximate.

Table 5.2
Kinetic Energy e-Folding Dissipation
Time Scale, for Mixed Layer Depth d = 20 m

$N_1 k$ ($s^{-1} m^{-1}$)	Case	T(inertial periods)
6.25×10^{-7}	3	13
1.25×10^{-6}	4	3.5
2.5×10^{-6}	5	1.25
5×10^{-6}	6	0.42

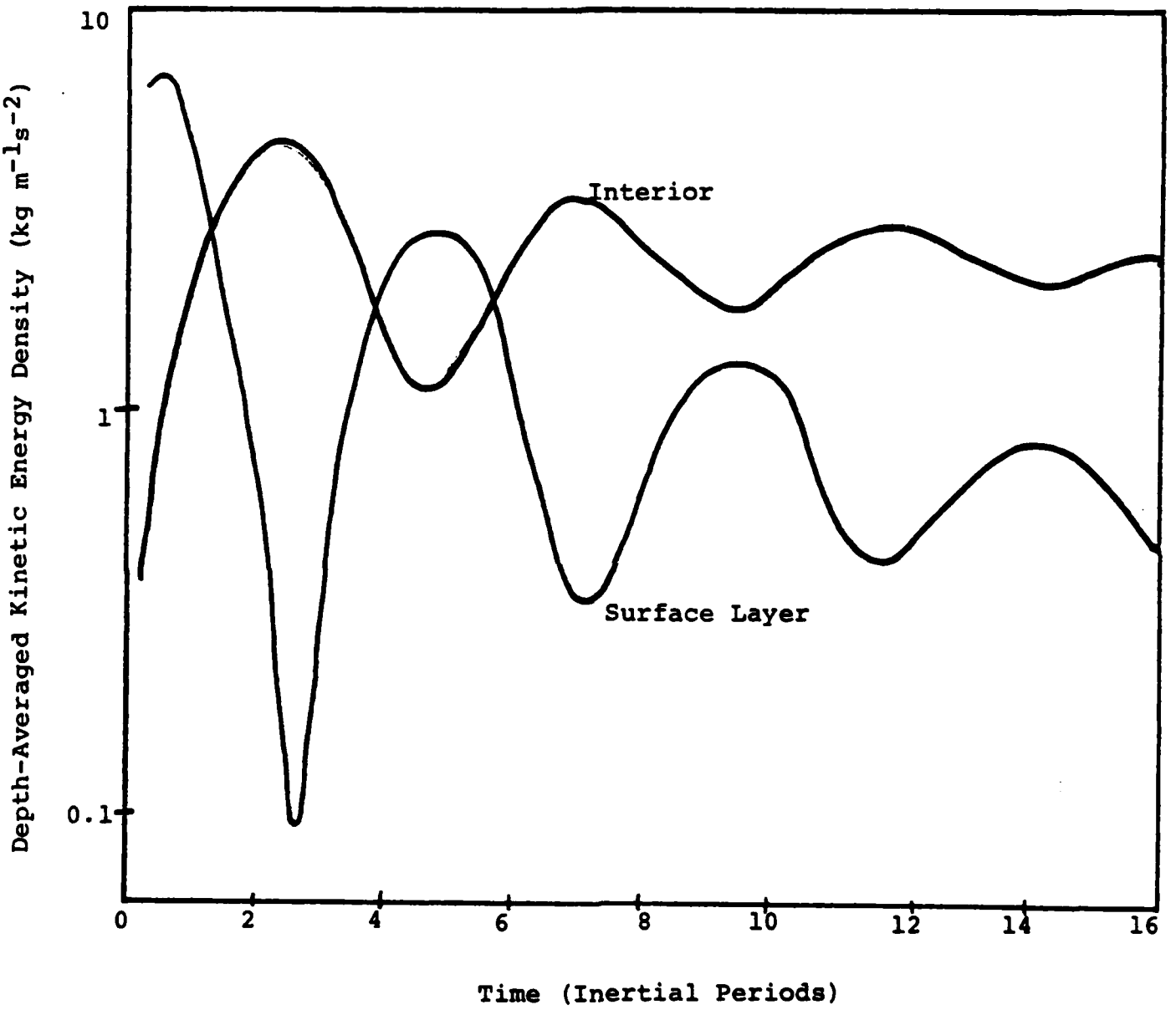

Fig. 5.4 Depth averaged kinetic energy in the surface layer $0.9 \leq z/D \leq 1.0$, and in the stratified interior layer $0.8 \leq z/D \leq 0.9$, for Case 2.

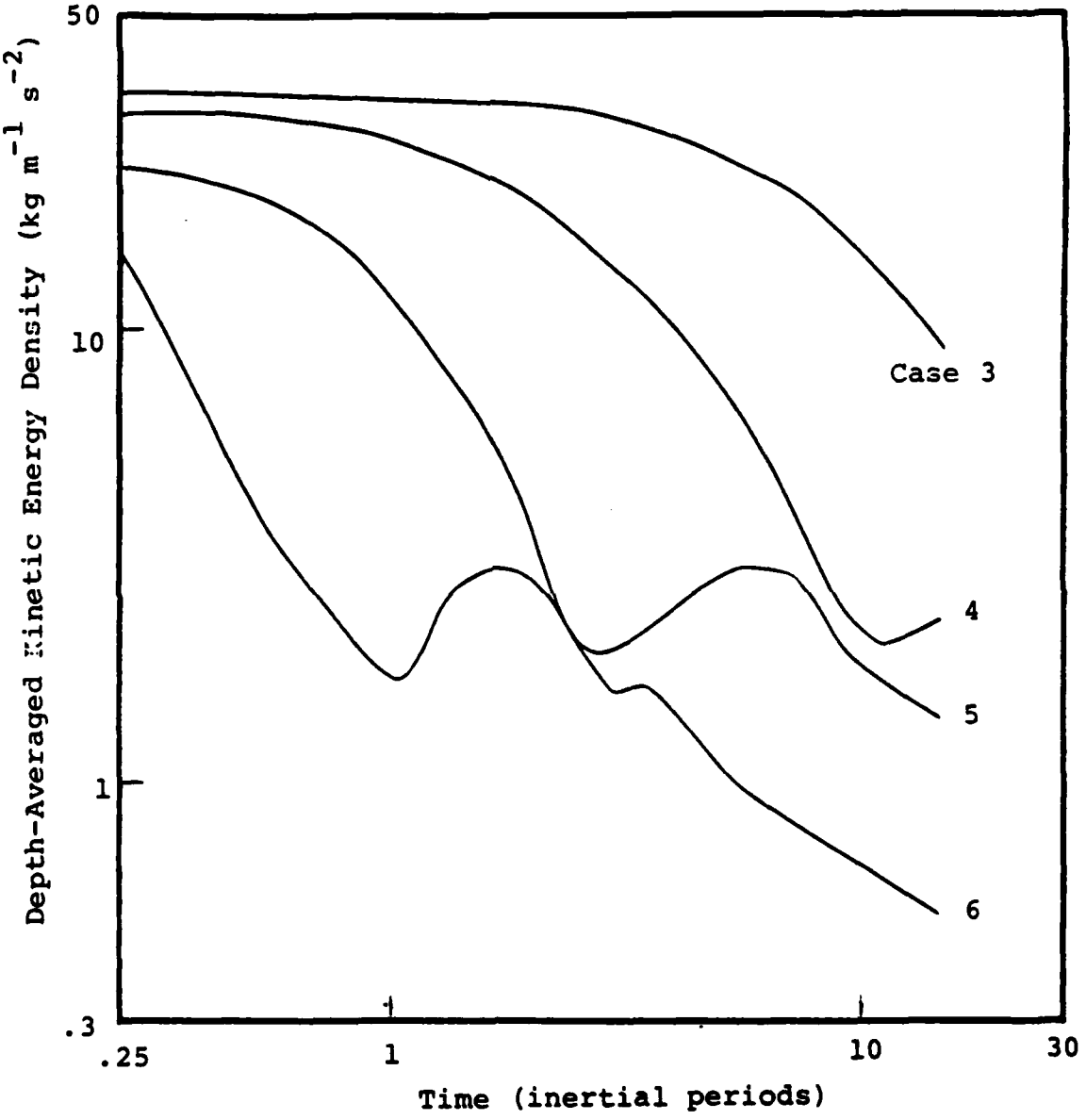

Figure 5.5 Depth-averaged kinetic energy density in the surface layer for Cases 3, 4, 5, 6 with N_1k = 6.25 x 10^{-7}, 1.25 x 10^{-6}, 2.5 x 10^{-6}, and 5 x 10^{-6} $s^{-1}m^{-1}$, respectively.

An approximate empirical formula for the dissipation time scale is

$$T(\text{inertial periods}) \approx (3 \times 10^{-6}/N_1 k)^{1.7}. \qquad (5.2)$$

The dissipation time scale given by (5.2) is greater than that in (4.11), but we remind the reader that N_o in (4.11) refers to a **uniform** stratification, while N_1 in (5.2) refers to the **peak** level of stratification.

As in Section 4.4, we can express a generalized formula for the dissipation time scale, in units of days, as follows:

$$T(\text{days}) \approx \frac{1}{\sin\theta}\left[\frac{\sin\theta\ \lambda(m)}{208\ N_1(\text{cph})\ d(m)}\right]^{1.7}. \qquad (5.3)$$

Table 5.3 is a tabulation of (5.3), for representative values of λ and N_1. Blank areas in the table are out of the parameter range covered by Cases 3-6. Typical values for N_1 are of order 20 cph. With this value, inertial oscillations produced by wind fields with dominant wavelengths less than 200 km are all dispersed from the surface layer within a few days.

These results cannot be readily generalized to Vaisala frequency profiles with parameters different from those listed for Cases 3-6 in Table 5.1. The strength of the

"frequency interference effect" depends on the relative amplitude of the peak of the Vaisala frequency distribution

Table 5.3

Kinetic Energy e-Folding Dissipation Time Scale (days), for Latitude θ = 40°N and Mixed Layer Depth d = 20m

		λ (km) 25	50	100	200
N_1(cph)	5	1.0	3.3	10.6	
	10	0.3	1.0	3.3	10.6
	20		0.3	1.0	3.3
	30			0.5	1.6

(the parameter a in (5.1)). When a=1, the problem reverts back to the uniform stratification profile discussed in Section 4. As a increases, the "frequency interference effect" becomes progressively stronger.

The resonant frequency of the interference effect depends on the magnitude $N_1 k$, as well as on the pycnocline thickness parameter c. The dependence of the resonant frequency ω_r on $N_1 k$ can be estimated for the particular cases illustrated in Figure 5.5

$$\omega_r = f[1 + (2.4 \times 10^5 N_1 k)^2]^{1/2}. \qquad (5.4)$$

The dependence of the resonant frequency on the pycnocline thickness is presented in Figure 5.6, which shows the time evolution of depth averaged kinetic energy in the surface layer for Cases 7-9. These cases are identical except in their pycnocline thickness parameter c. The dissipation rate

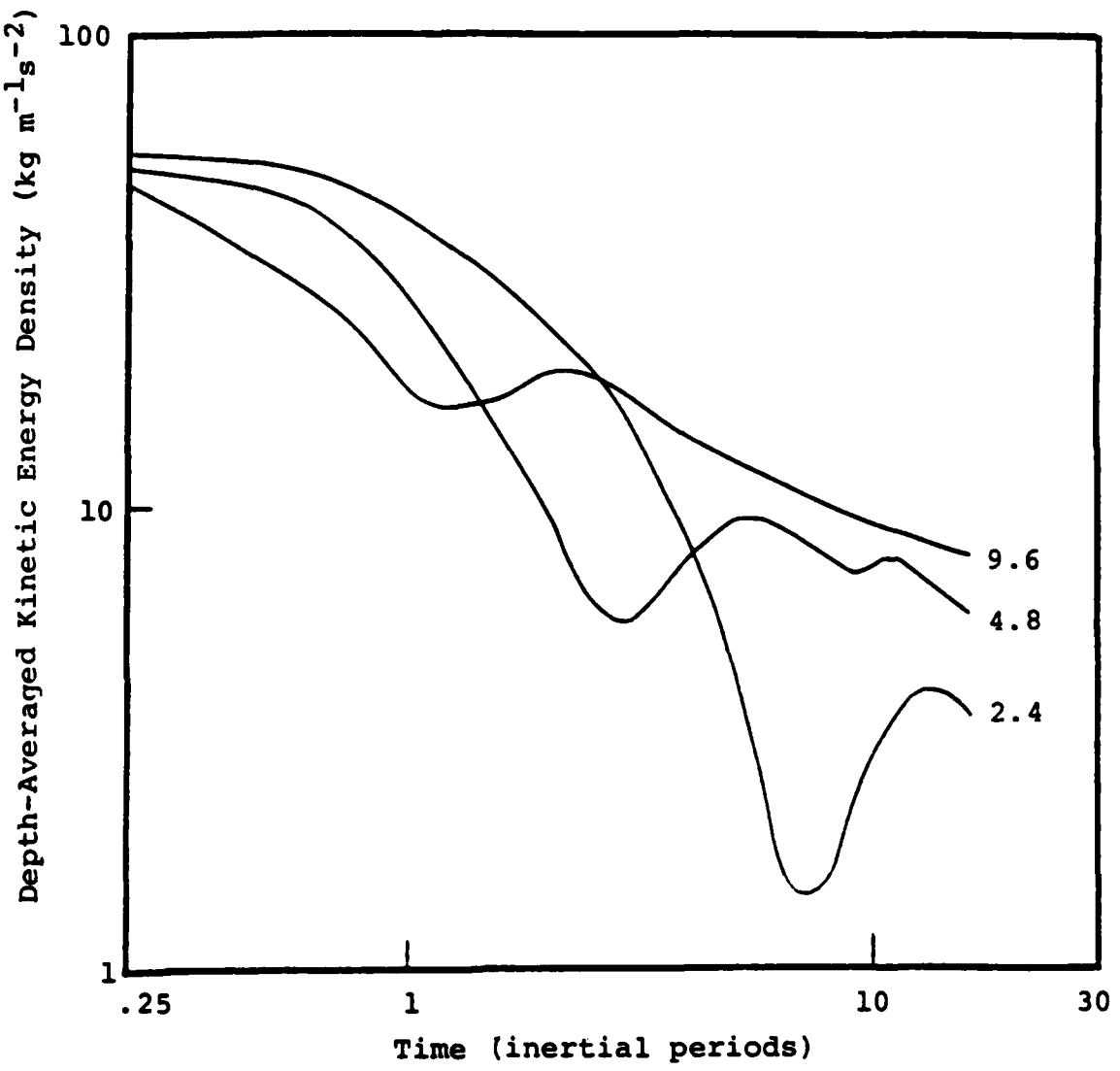

Figure 5.6 Depth-averaged kinetic energy density in the surface layer for Cases 7-9, with pycnocline thickness parameter c = 2.4, 4.8, 9.6 m.

initially increases with increasing c. The reason is that with c increasing, the high stratification region extends to a greater depth, and allows faster vertical dispersion. After some time has elapsed, the wave component whose vertical wavelength is resonant with the peak in the Vaisala frequency distribution reaches the strong pycnocline, and interferes with the dominant inertial oscillations in the surface layer. The frequency of this interference effect increases with increasing pycnocline thickness. The amplitude of the interference effect (that is, the amplitude of the kinetic energy oscillation in absolute terms) is independent of the pycnocline thickness, c. After the resonant wave component has had time to propagate into the uniformly stratified region, the dissipation of surface layer kinetic energy continues, at a rate independent of c.

5.3 MODEL-DATA COMPARISON: BALTIC SEA

In this section we present a qualitative comparison between the model results and current meter observations in the Baltic Sea. The observations were taken at 56°05.7'N, 18°44.4'E, a location where the bottom depth is 105 m, and are described by KRAUSS (1981). Current meters were deployed at 10 m intervals between the depths 30 and 100 m.

Figure 5.7 shows the u-component of velocity from 8 September to 21 September 1977, from KRAUSS (1981). Three storms occurred during this interval, a relatively weak one with wind speeds up to 22 m/sec on 10 September, and two stronger storms with wind speeds up to 29 m/sec on 12 and 14 September. We wish to concentrate our attention on the interval from 12 to 16 September. During this interval, the base of the mixed layer deepened from about 25 to 30 m, as shown in the smoothed temperature distribution in Figure 5.8.

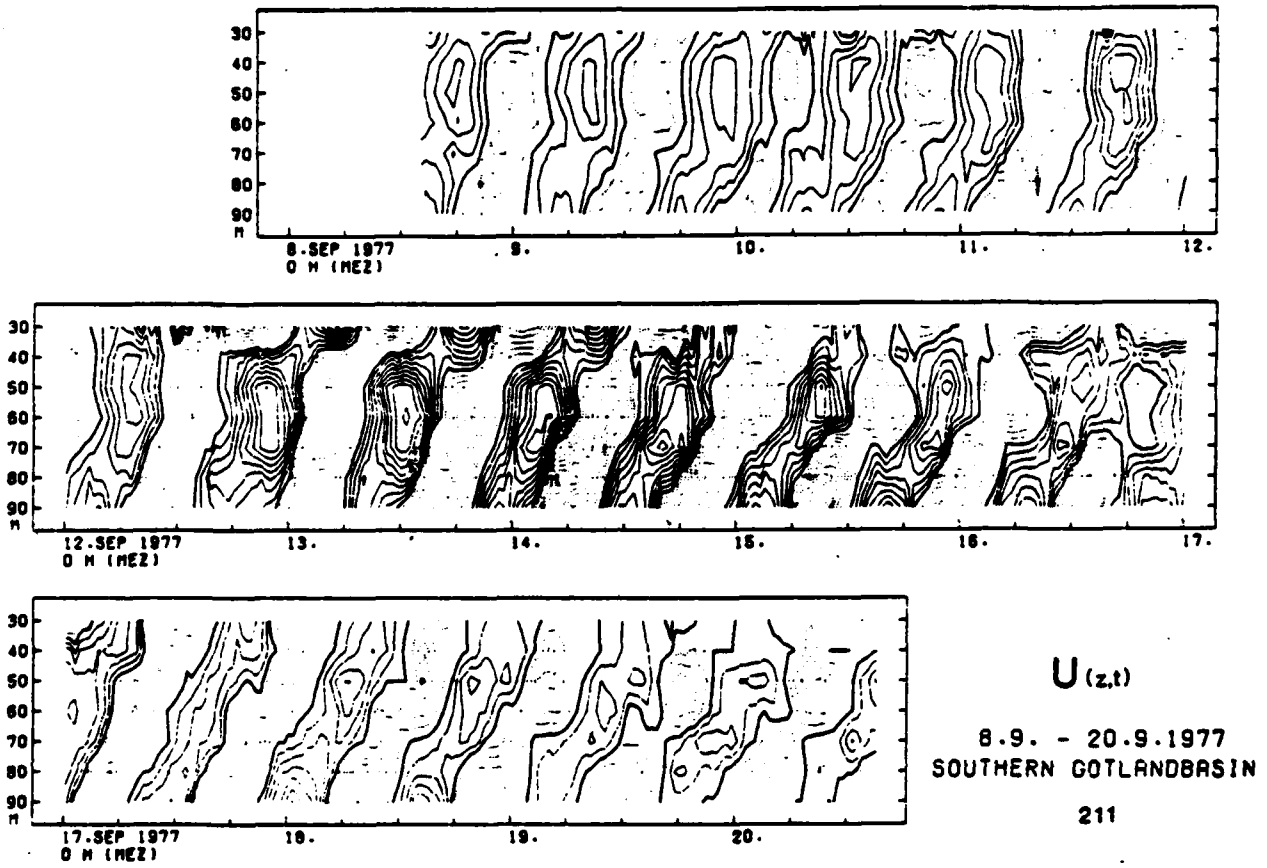

Figure 5.7 U-component of velocity in the Baltic Sea during the time interval 8-20 September, 1977, from KRAUSS (1981). Contour intervals are plotted for every 5 cm/sec. Heavy line is zero velocity; full lines are positive and dashed lines, negative.

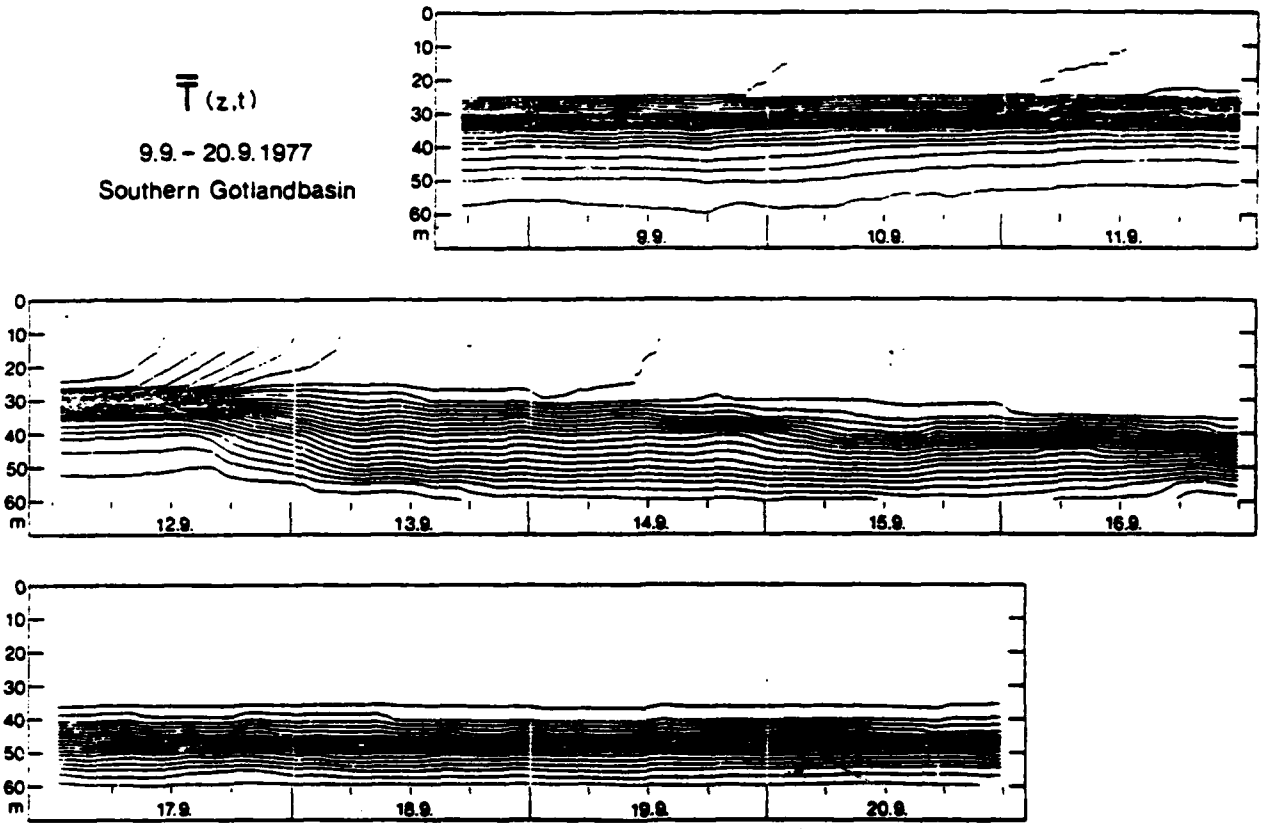

Figure 5.8 Smoothed temperature distribution in the Baltic Sea from 8-20 September, 1977, from KRAUSS (1981). Isotherms are plotted every 0.5°C.

The storm on 12 September increased the amplitudes of the inertial waves, while the phase of the storm on 14 September was such as to reduce the amplitudes somewhat. During the interval 12 to 16 September there is a definite trend toward smaller vertical phase velocities. In other words, the bands of constant phase increasingly slope away from the vertical. This feature, plus the abrupt change in phase from the mixed layer to the thermocline (seen more clearly in Krauss' Figure 11, but not shown here) are strikingly similar to the model results in Figure 5.2.

In a shallow bottom sea, bottom reflections become important several inertial periods after a wind event has occurred. From about 15 to 16 September (as well as on 19 September) there are indications of bottom reflections. These reflections show up as a sharp phase shift at about 70 m depth. This phase shift is similar to that which develops in Figure 5.2 (Case 1) about 3 inertial periods after the wind impulse.

5.4 MODEL-DATA COMPARISON: DEEP OCEAN

In this section we present a qualitative comparison between our model results and current observations in the deep ocean. For this comparison, we consider the Mixed Layer Experiment (MILE) which was carried out in the northeastern Pacific Ocean near Ocean Weather Station P. The MILE-1 mooring, located at 49°37'N, 145°6'W was connected to a surface float in 4360 m of water. A complete description of the MILE setting may be found in DAVIS et al. (1981). The MILE-1 mooring collected data over a 20-day period, from 19 August to 7 September. Current meters collected data samples at a rate of 32 hr^{-1}, which we filtered to 1 hr^{-1}.

Figure 5.9 shows a contour plot of the u component of velocity. As the two uppermost current meters delivered incomplete records, the depth range covered by these plots is from 11 to 121 m. Inertial oscillations dominate much of the 20-day records. The inertial period at this latitude is about 17 hr. Vertical shear, marked by an abrupt change in phase, is concentrated near the top of the thermocline, at a depth of about 40 m. Below 40 m, the bands of constant phase are for the most part nearly vertical. The most significant exception is from 29-30 August, when the phase progression is downward. The implication is that the propagation direction of a local internal wave packet is upward.

Figure 5.10 shows the wind stress components during MILE, reproduced from DAVIS et al. (1981). Two major wind events occurred, on 21-24 August and 30 August-1 September. Both of these wind events generated inertial oscillations in the mixed layer, during 22-23 August and 1-3 September, respectively.

Both in the mixed layer and below, the inertial oscillations are intermittent, and decay within about 2 days after their generation. Their peak amplitudes are about 20-30 cm sec^{-1}. The strongest peak amplitudes in the mixed layer occur on 20 August, 23 August, 25 August, 2 September, and 5 September, and the strongest peak amplitudes in the thermocline occur on 19 August, 21-22 August, 24 August, and 6 September. There seems to be a 2-3 day cycle, in which strong inertial waves oscillate between the mixed layer and upper seasonal thermocline. This oscillation is similar in character to the model-predicted frequency interference effect, described in Section 5.2. The peak amplitudes which occur in the mixed layer on 20 August, 25 August, and

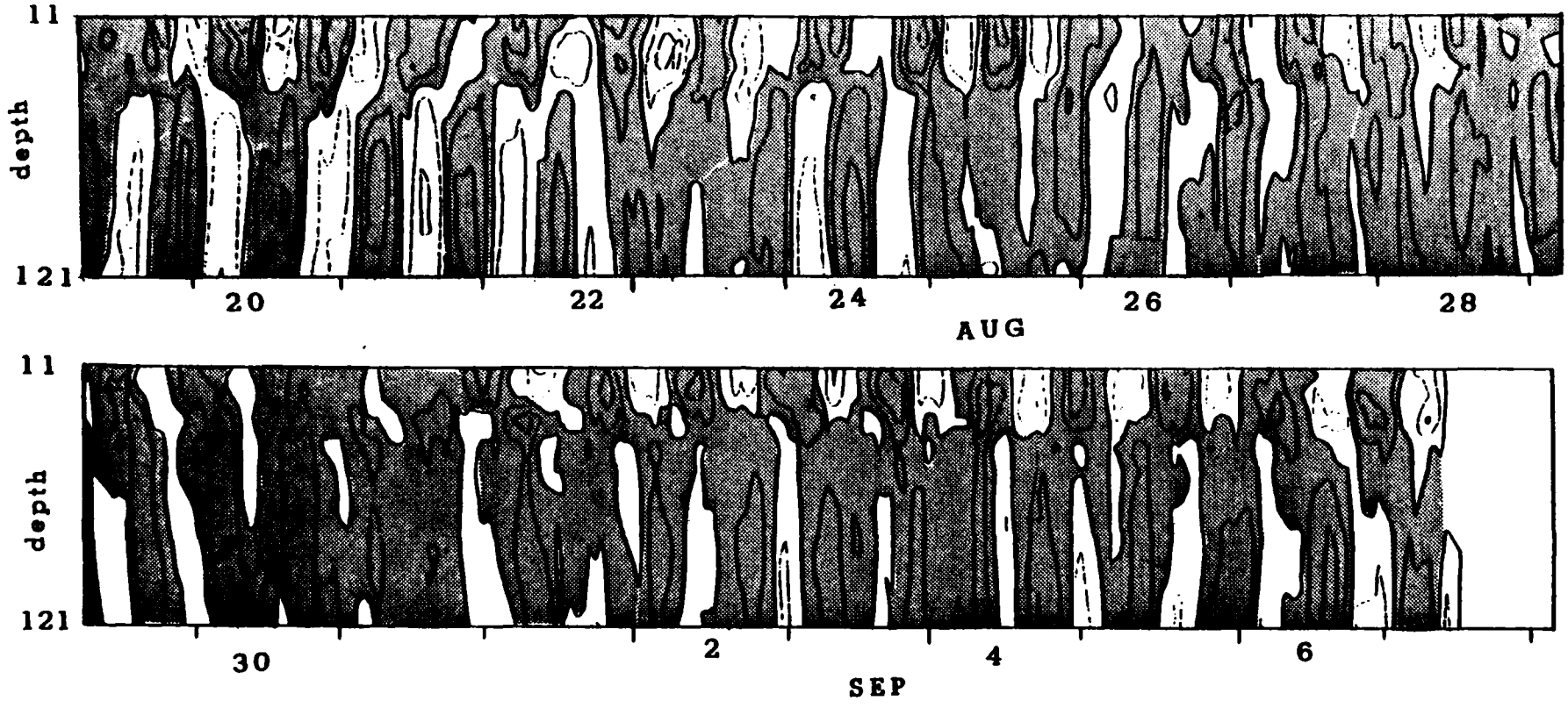

Figure 5.9 U-component of velocity during MILE from 19 August to 7 September, 1977. Depth ranges from 11 m to 121 m. Shaded areas are positive (eastward) and unshaded areas are negative. Thin dashed contour lines are spaced at 10 cm/sec increments.

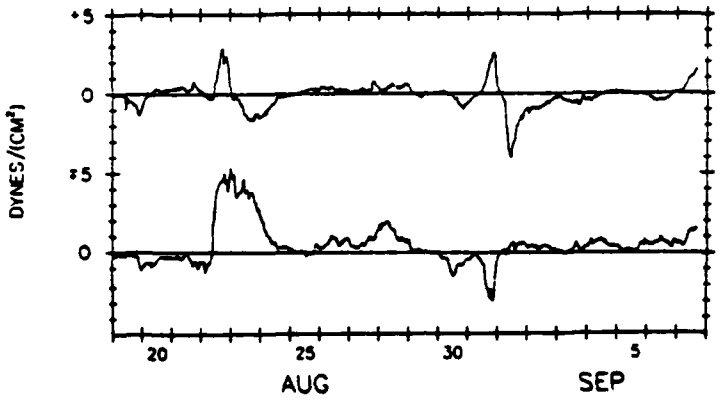

Figure 5.10 Wind stress to the north (upper trace) and to the east (lower trace) at Station P from 19 August to 7 September, 1977. From DAVIS et al. (1981).

5 September do not seem to result directly from wind events. This observation lends support to the hypothesis that the frequency interference effect is responsible for these oscillations.

Section 6
SUMMARY AND RECOMMENDATIONS

During FY81, we developed a linear model of inertial waves in a shallow sea (Rubenstein 1981b, 1982). This model predicted the near-inertial frequency response of the ocean to wind events. The model equations were solved with a Fourier-Chebyshev expansion in the spatial dimensions, and numerically in time. Delta-function wind stress impulses were applied at the surface. The response in the shallow sea was shown to be governed by vertical modes. The frequencies of these modes satisfied the internal wave dispersion relation.

During FY82, we extended this model to the deep ocean, as described in this report. While the equations are very similar to those of KRAUSS (1978, 1979), we have introduced a porous damping region which minimizes reflections from the bottom of the computational domain. Thus, the model simulates an ocean of "infinite" depth. Vertical modes associated with standing waves, prevalent in our earlier solutions, do not develop in this model. We successfully validated the model against analytic solutions of the diffusion problem.

We applied this model to determine the rate at which inertial oscillations in the surface layer are dissipated. We looked first at a uniformly stratified ocean. High frequency internal wave components had the fastest group velocities, and immediately after a wind event they left the surface layer soonest. Lower frequency, near-inertial waves were left behind, and propagated downward much more slowly. The dissipation rate of surface layer kinetic energy is a

function of the ratio $Nd/f\lambda$, where λ is the horizontal wavelength of the wind event (a front or storm system), d is the mixed layer depth, f is the local inertial frequency, and N is the dimensional Vaisala frequency, a measure of the stratification.

We also considered a more realistic nonuniform stratification distribution, with a strong inviscid pycnocline immediately below a diffusive surface layer. For cases where the peak Vaisala frequency was of order 20 cph, and the wavelength associated with the wind event was less than 200 km, the kinetic energy in the surface layer dissipated within a few days. This result is in agreement with simple mixed layer inertial oscillation prediction models (POLLARD and MILLARD, 1970; KUNDU, 1976; POLLARD, 1980). These models show the best agreement with observational data when their damping factors correspond to e-folding decay times (for the amplitude of inertial oscillations) in the range 2 to 8 days. Therefore, vertical dispersion alone is adequate to account for the observed dissipation rates.

When a sufficiently peaked pycnocline is present, a frequency interference effect occurs. A particular low frequency wave component resonates within the pycnocline, and interferes with the dominant inertial oscillations in the surface layer. The strength of the interference depends on the peakedness of the pycnocline. The resonant frequency depends on the stratification and thickness of the pycnocline. As a result of this effect, the kinetic energy in the surface layer may not dissipate monotonically. Energy may be alternately exchanged between the surface layer and the pycnocline immediately below. We examined deep-ocean observations taken during MILE, and found some evidence of

this frequency interference effect. Several of the incidences of inertial oscillations in the mixed layer did not seem to result directly from any particular local wind event. Instead, kinetic energy was cyclically exchanged between the surface layer and the upper seasonal thermocline. The cycle period was 2 to 3 days.

We also compared model simulations with current meter observations in the shallow (105 m) Baltic Sea. We found that vertical phase velocity generally decreases after the occurrence of a storm. Our comparisons reveal that bottom reflections become important after a few inertial periods have elapsed after a storm.

A number of ocean mixed-layer prediction models incorporate damping factors which parameterize the dispersion of near-inertial internal waves (POLLARD and MILLARD, 1970; KUNDU, 1976; CLANCY et. al., 1981). The magnitudes of these damping factors are known to vary with changing environmental conditions, but are determined through the method of obtaining a "best fit" with a data set. The results of the present study should allow investigators to parameterize the dispersion of internal waves with better accuracy.

One such mixed-layer model, known as TOPS (Thermodynamical Ocean Prediction System) was developed at the Naval Ocean Research and Development Activity for operational use at the Navy's Fleet Numerical Oceanography Center. TOPS is used to predict the ocean mixed-layer environment over large geographical regions. TOPS incorporates damping factors which determine the rate of attenuation of inertial oscillations in the mixed-layer. Using the results of the present

study, it may be possible to construct a more realistic parameterization of the attenuation rate, which depends on the local environment.

The model described in this report is linear; as a result, the profiles of eddy diffusivity and Vaisala frequency are constant in time. It would be more realistic to include turbulent buoyancy fluxes and to allow the Vaisala frequency profile to evolve with time. The eddy diffusivity could be parameterized in terms of the local shear, or Richardson number. We recommend that the current model be extended to include these changes. In this way, we should obtain better insight into the dynamics of the upper ocean in the aftermath of the passage of wind events and storms.

REFERENCES

BELL T. H. (1978) Radiation damping of inertial oscillations in the upper ocean. Journal of Fluid Mechanics, 88, 289-308.

CARBONE R. E. (1982) A severe frontal rainband. Part I: Stormwide hydrodynamic structure. Journal of the Atmospheric Sciences, 39, 258-279.

CLANCY R. M., P. J. MARTIN, S. A. PIACSEK, and K. D. POLLAK (1981) Test and evaluation of an operationally capable synoptic upper-ocean forecast system. Naval Ocean Research and Development Activity, Technical Note 92, 63 pp.

DAVIS R. E., R. DESZOEKE, D. HALPERN, and P. NIILER (1981) Variability in the upper ocean during MILE. Part I: The heat and momentum balances. Deep-Sea Research, 28, 1427-1451.

GONELLA J. (1971) A local study of inertial oscillations in the upper layers of the ocean. Deep-Sea Research, 18, 775-788.

HOBBS P. V., T. J. MATEJKA, P. H. HERZEGH, J. D. LOCATELLI, and R. A. HOUZE, JR. (1980) The mesoscale and microscale structure and organization of clouds and precipitation in midlatitude cyclones. I: A case study of a cold front. Journal of the Atmospheric Sciences, 37, 568-596.

HOBBS P. V. and P. O. G. PERSSON (1982) The mesoscale and microscale structure and organization of clouds and precipitation in midlatitude cyclones. Part V: The substructure of narrow cold-frontal rainbands. Journal of the Atmospheric Sciences, 39, 280-295.

KRAUSS W. (1978) The response of a stratified viscous sea to moving meteorological fronts and squall lines. Deutche Hydro. Zeitsch., 31, 16-30.

KRAUSS W. (1979) Inertial waves in an infinite channel of rectangular cross section. Deutche Hydro. Zeitsch., 32, 248-266.

KRAUSS W. (1981) The erosion of a thermocline. Journal of Physical Oceanography, 11, 415-433.

KROLL J. (1975) The propagation of wind-generated inertial oscillations from the surface into the deep ocean. Journal of Marine Research, 33, 15-51.

KUNDU P. K. (1976) An analysis of inertial oscillations observed near the Oregon Coast. Journal of Physical Oceanography, 6, 879-893.

LEBLOND P. H. and L. A. MYSAK (1978) Waves in the Ocean. Elsevier Scientific Publishing Company, New York, 602 pp.

PERKINS, H. (1970) Inertial oscillations in the Mediterranean. Ph.D. thesis, MIT-Woods Hole, 155 pp.

POLLARD R. T. (1970) On the generation by winds of inertial waves in the ocean. Deep-Sea Research, 17, 795-812.

POLLARD R. T. (1980) Properties of near-surface inertial oscillations. Journal of Physical Oceanography, 10, 385-398.

POLLARD R. T. and R. C. MILLARD, JR. (1970) Comparison between observed and simulated wind-generated inertial oscillations. Deep-Sea Research, 17, 813-821.

ROBERTS G. O and D. RUBENSTEIN (1980) Shear effects on internal gravity wave propagation. SAI Report No. 81-244-WA, Science Applications, Inc., McLean, VA.

RUBENSTEIN D. (1981a) Models of near inertial vertical shear. Science Applications, Inc., Ocean Physics Division, McLean, VA. SAI-82-546-WA.

RUBENSTEIN D. (1981b) A dynamical model of wind-induced near-inertial motions. Science Applications, Inc., Ocean Physics Division, McLean, VA. SAI-82-598-WA.

RUBENSTEIN D. (1982) Near-inertial motions: A preliminary model-data comparison. Science Applications, Inc., Ocean Physics Division, McLean, VA. SAI-82-620-WA.

SCHOTT F. (1971) Spatial structure of inertial-period motions in a two-layered sea, based on observations. Journal of Marine Research, 29, 85-102.

THOMPSON R. E. and W. S. HUGGETT (1981) Wind-driven inertial oscillations of large spatial coherence. Atmosphere-Ocean, 19, 281-306.